HAL
open science

Magnetic properties of variably serpentinized abyssal peridotites

Omar Oufi, Mathilde Cannat, Hélène Horen

To cite this version:

Omar Oufi, Mathilde Cannat, Hélène Horen. Magnetic properties of variably serpentinized abyssal peridotites. Journal of Geophysical Research : Solid Earth, 2002, 107 (B5), pp.EPM 3-1-EPM 3-19. 10.1029/2001JB000549 . insu-02177970

HAL Id: insu-02177970

https://insu.hal.science/insu-02177970v1

Submitted on 9 Jul 2019

HAL is a multi-disciplinary open access archive for the deposit and dissemination of scientific research documents, whether they are published or not. The documents may come from teaching and research institutions in France or abroad, or from public or private research centers.

L'archive ouverte pluridisciplinaire **HAL**, est destinée au dépôt et à la diffusion de documents scientifiques de niveau recherche, publiés ou non, émanant des établissements d'enseignement et de recherche français ou étrangers, des laboratoires publics ou privés.

Magnetic properties of variably serpentinized abyssal peridotites

Omar Oufi and Mathilde Cannat
Laboratoire de Géosciences Marine, CNRS/IPGP, Paris, France

Hélène Horen
Laboratoire de Géologie, Ecole Normale Superieure, Paris, France

Received 30 March 2001; revised 23 October 2001; accepted 28 October 2001; published 21 May 2002.

[1] We have compiled new and published data on the magnetic properties of 245 serpentinized abyssal peridotites from seven Deep Sea Drilling Project and Ocean Drilling Program sites. The magnetic susceptibility (K) of these samples does not increase linearly with the degree of serpentinization (S). Instead, K remains modest in partially serpentinized samples ($S < 75\%$) and then increases rapidly. The rate of formation of magnetite during serpentinization increases as the iron content of serpentine minerals decreases: ~6% FeO in the first stages of serpentinization and only 2–3% FeO as serpentinization proceeds beyond $S \sim 75\%$. Contrasting remanent behaviors observed in extensively serpentinized samples (some samples have natural remanent magnetizations (NRM) comparable to those of basalts, while other samples have low NRM values, for similarly high K values) are due to differences in the effective magnetic grain size and appear related to serpentine textures. Samples with small effective magnetic grain sizes have a well-developed serpentine meshwork, outlined by thin vein-like magnetite concentrations. Most serpentinized abyssal peridotites have this well-developed serpentine mesh texture. We thus propose that high NRM (4–10 A/m on average) and K (~0.07 SI on average) are the most likely signature for extensively serpentinized ($S > 75\%$) peridotites in the oceanic crust. Moderately serpentinized peridotites ($S < 75\%$) have NRM values <5 A/m and $K < 0.05$ SI. Low-temperature oxidation of magnetite is found to lower the NRM and K values of seafloor samples and of cataclastically deformed drilled samples. *INDEX TERMS:* 1517 Geomagnetism and Paleomagnetism: Magnetic anomaly modeling; 1540 Geomagnetism and Paleomagnetism: Rock and mineral magnetism; 3035 Marine Geology and Geophysics: Midocean ridge processes; 3660 Mineralogy and Petrology: Metamorphic petrology; *KEYWORDS:* Serpentinization, rock magnetism, marine magnetic anomalies, magnetite, serpentinite

1. Introduction

[2] Unaltered peridotites have very weak magnetic susceptibilities ($<10^{-3}$ SI [*Toft et al.*, 1990]), and their magnetic behavior is paramagnetic. Extensively serpentinized peridotites, by contrast, have high magnetic susceptibilities (up to ~0.15 SI [*Krammer*, 1990]), and their magnetic behavior is ferromagnetic. This change in magnetic properties is due to the formation of magnetite during serpentinization [e.g., *Dunlop and Prévot*, 1982]. Magnetite is formed to host the excess iron that is released by ferromagnesian minerals (olivine and pyroxenes) and is not accommodated in the serpentine structure or washed out of the rock by fluids [*Moody*, 1976; *Wicks and Whittaker*, 1977; *Komor et al.*, 1985]. In the course of serpentinization, peridotites also acquire a crystallization remanence (CRM) because of the growth of newly formed magnetite grains in the ambient geomagnetic field [*Dunlop and Prévot*, 1982; *Smith and Banerjee*, 1985; *Bina and Henry*, 1990].

[3] The magnetic susceptibility of serpentinized peridotites increases with increasing modal amounts of magnetite and has been proposed to be linearly correlated with the degree of serpentinization [*Bina and Henry*, 1990; *Nazarova*, 1994]. However, measurements of magnetic susceptibility and density (a parameter that decreases linearly with increasing degrees of serpentinization [*Christensen*, 1972; *Miller and Christensen*, 1997]) in serpentinized peridotites from ophiolitic massifs show that the evolution of modal magnetite contents with the degree of serpentinization is not linear [*Toft et al.*, 1990; *Horen and Dubuisson*, 1995]. The observed density-susceptibility trends can be modeled [*Toft et al.*, 1990] by a multistage process that involves a succession of serpentinization reactions such that the production rate of magnetite increases with the degree of serpentinization. The evolution of magnetic susceptibilities with increasing degrees of serpentinization has been shown to follow a similarly nonlinear, but distinct trend in samples from Ocean Drilling Program (ODP) site 895 at Hess Deep [*Kelso et al.*, 1996]. This evolution remains to be characterized in other sets of abyssal peridotites.

[4] Remanent magnetic properties of abyssal serpentinized peridotites that determine their ability to contribute to the marine record of past magnetic inversions have been reviewed by *Dunlop and Prévot* [1982] and *Nazarova* [1994]. Since then a lot more data have become available, showing that natural remanent magnetization (NRM) values for abyssal peridotites are highly variable. For example, extensively serpentinized peridotite samples from ODP site 920 near the Mid-Atlantic Ridge (MAR) have NRM values similar to the values measured in mid-ocean ridge basalts (10–20 A/m [*Cannat et al.*, 1995]). By contrast, extensively serpentinized peridotite samples from ODP site 670, some 18 km south of ODP site 920, have lower NRM values (between 1.5 and 5 A/m [*Bina and Henry*, 1990; *Krammer*, 1990]). The causes for such contrasting remanent behavior remain to be investigated.

[5] Understanding the magnetic properties of variably serpentinized peridotites could be important for the interpretation of marine magnetic anomalies because these rocks are commonly exposed in

Copyright 2002 by the American Geophysical Union.
0148-0227/02/2001JB000549$09.00

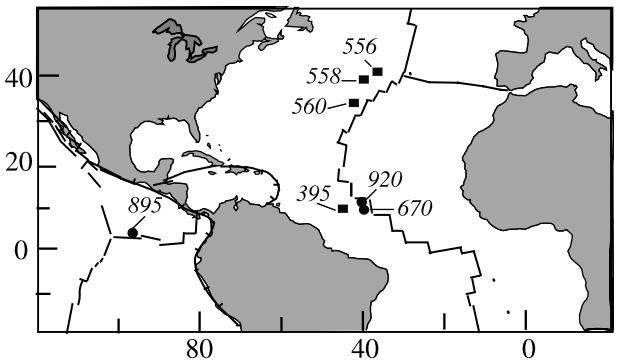

Figure 1. Map showing the location of DSDP (solid squares) and ODP (solid circles) sites considered in this study. DSDP sites 556 (~35 Myr), 558 (~35 Myr), and 560 (~18 Myr) are located near the Azores. DSDP site 395 (~7 Myr) and ODP sites 670 (<1 Myr) and 920 (<1 Myr) are located near the Mid-Atlantic Ridge south of the Kane Fracture Zone. ODP site 895 (<1 Myr) is located in the Hess Deep, near the East Pacific Rise.

the seafloor of slow spreading oceans [*Lagabrielle and Cannat*, 1990; *Cannat*, 1993]. The magnetic record of the slow spreading MAR is strongly segmented, and the inside corners of axial discontinuities (corner bounded by the ridge and the active offset) and their off-axis traces are commonly marked by more positive magnetization [*Pockalny et al.*, 1995; *Pariso et al.*, 1996; *Tivey and Tucholke*, 1998]. Serpentinized peridotites are commonly sampled at such inside corner settings and have been proposed to carry a strong induced magnetization that could be the cause of the observed positive magnetization anomalies [*Pariso et al.*, 1996; *Tivey and Tucholke*, 1998]. Magnetic anomalies recorded in crust formed at slow spreading ridges also commonly differ in both amplitude and skewness from the predictions of synthetic models that use a thin source layer of constant magnetization inferred to represent the extrusive upper crust [e.g., *Talwani et al.*, 1971]. The anomalous skewness of marine magnetic anomalies has been shown to increase at decreasing spreading rates [*Roest et al.*, 1992]. This increase has been attributed to the increasing contribution of serpentinized peridotites in the lower crust and upper mantle to the remanent magnetic signal [*Dyment and Arkani-Hamed*, 1995; *Dyment et al.*, 1997]. Improved modeling of this possible effect and of the along-axis variations of the magnetic signal at slow spreading ridges requires both better constraints on the abundance and degree of serpentinization of peridotites in slow spreading oceanic lithosphere and a better understanding of the variability of the induced and remanent magnetic properties of abyssal serpentinized peridotites.

[6] In this paper, we present a compilation of published and new data on the magnetic properties of abyssal peridotites from six Deep Sea Drilling Project (DSDP) and ODP sites drilled near the MAR and from ODP site 895 drilled in the Hess Deep near the East Pacific Rise (EPR; Figure 1). The questions we address are the following: (1) How does the degree of serpentinization affect the magnetic susceptibility of abyssal peridotites? (2) What factors control the remanent properties of serpentinized abyssal peridotites? To address these questions, we adopt a multidisciplinary approach, using density measurements to estimate the degrees of serpentinization and looking in samples selected for their contrasting magnetic behaviors for systematic differences in textures, in the chemistry of serpentine minerals, and in the distribution of magnetite in the serpentine network.

2. Analytical Methods

[7] We have only considered drilled samples, as opposed to dredged samples and samples collected during submersible dives. This is because most seafloor samples of serpentinized peridotites have been subjected to extensive low-temperature oxidative alteration of magnetite (maghemitization) that modifies their magnetic properties [*Smith and Banerjee*, 1985]. We found that this alteration is significantly reduced in most drill holes, just a few meters below seafloor.

2.1. Magnetic Properties and Density

[8] We have compiled published magnetic and density data from a variety of sources (see Table 1), carefully checking the mineralogy of each sample, directly on the cores archived in DSDP and ODP core repositories (Lamont-Doherty Earth Observatory, Texas A&M University, and Bremen University core depositories) and on thin sections borrowed from the DSDP and ODP archives or cut from newly obtained samples. Mean values quoted are arithmetic means.

[9] Additional magnetic and density data have been obtained on minicores (diameter 12 mm; length 15 mm). Thermomagnetic curves have been determined using the Kappabridge instrument (KLY 3) of the Ecole Normale Supérieure (Paris). Temperature was monitored with a thermocouple in contact with the sample, and the sample chamber was filled with argon to purge the system of oxygen. Magnetic susceptibility was measured with this same Kappabridge instrument. For natural remanent magnetization (NRM) we used the JR5 spinner magnetometer of the Ecole Normale Supérieure, Paris. Magnetic hysteresis parameters were determined on minicores at the Laboratoire de Géomagnétisme de St. Maur, with a translation magnetometer built by M. Legoff. A field of 600 mT was sufficient to reach magnetic saturation of our samples. For the density measurements the samples were submerged in water and placed in a vacuum for 3 days in order to saturate microfractures and open pore spaces. Density was then measured using a microbalance (precision $\pm 10^{-4}$ g) and a pyctometer for measuring sample volume.

2.2. Mineralogy and Mineral Chemistry

[10] X-ray diffraction spectra have been obtained on powders with the Inel X-ray diffractometer of the Muséum National d'Histoire Naturelle (Paris), using a copper anticathode (50 kV, 32 mA), CuKa radiation, and a mixture of quartz and boehmite to calibrate the diffractometer. Mineral chemistry data have been acquired on a CAMEBAX electron microprobe (CAMPARIS, Université de Paris VI), using a current of 10 nA, 15 kV tension, counting times of 10–20 s, and a beam ~10 μm in diameter.

2.3. SEM Images of Magnetite Grains and Aggregates

[11] The size and distribution of magnetite grains, and clusters of grains, in the serpentine network have been analyzed with the NIH Image 1.61 software (developed by the U.S. National Institute of Health), on reflectivity images obtained with the JEOL JSM-840 scanning electron microscope (SEM) of Université de Paris VI.

3. Provenance and Petrographic Characteristics of the Samples

3.1. Location of Drill Sites

[12] The 245 samples considered in this paper (Table 1) come from seven DSDP and ODP drill sites (Figure 1). Three sites (DSDP sites 556, 558, and 560; leg 82) have been drilled in crust 18 to 35 Myr old on the west flank of the Mid-Atlantic Ridge (MAR) south of the Azores platform [*Bougault et al.*, 1985]. Three sites (DSDP site 395 and ODP sites 670 and 920; legs 45, 109, and 153) have been drilled in crust <1 Myr to ~7 Myr old to the west of the MAR south of the Kane Fracture Zone [*Melson et al.*, 1978; *Detrick et al.*, 1988; *Cannat et al.*, 1995]. One site (ODP site 895, leg 147 [*Mével et al.*, 1993]) was drilled in crust formed <1 Myr

Table 1. Magnetic Properties, Density, and Lithologies of Serpentinized Peridotite Drilled at DSDP Sites 395, 556, 558, and 560 and at ODP Sites 670, 895, and 920[a]

Hole	Sample	NRM, A/m	*K*, SI	Jrs, A m^2/kg	Js, A m^2/kg	Hc, mT	Hcr, mT	MDF, mT	*d*, g/cm^3	d_c, g/cm^3	*T*°C, °C	Lith	Ref[b]
556	13R1, 64–67[c]	0.19	0.020	0.38	1.26	22.50	43.88	33.00	2.64	2.60	Tirr(583)	SH	1
	20R2, 20–24[c]	0.07	0.037	0.13	2.21	11.60	19.95	24.40	2.67	2.61		SH	1
558	41R1, 60–63[c]	0.04	0.013	0.05	0.66	11.30	24.75	13.00	2.48	2.46		SH	1
	41R3, 66–69[c]	0.04	0.023	0.09	1.26	17.60	24.75		2.67	2.63		SH	1
	41R3, 113–117[c]	0.05	0.020	0.06	0.81	13.00	24.75	10.20	2.64	2.62	Tirr(583)	SH	1
	42R1, 122–125[c]	0.57	0.101	0.22	3.65	9.30	24.75	12.80	2.59	2.48		SH	1
	43R1, 8–11	2.62	0.068	0.20	1.51	9.20	24.75					SH	2
	43R1, 17–20[c]	0.36	0.080	0.17	4.19	7.50	24.75	8.20	2.51	2.38		SH	1
	43R1, 129–131[c]	0.33	0.078	0.21	3.56	9.10	24.75	8.20	2.53	2.42		SH	1
560	5R1, 98–101[c]	0.31	0.083	0.31	1.41	20.30	24.75		2.64	2.60		SH	1,2
	5R1, 109–112	1.10	0.069	0.20	0.86	18.80	24.75					SH	2
395	3R1, 89–91	1.02			5.20	12.50			2.62	2.47		SH	8
	4R2, 56–58	2.42			6.08	7.50			2.67	2.49		SH	8
	4R2, 64–66[c]	0.28	0.071	0.92	5.11	9.60	11.07	13.00	2.66	2.51		SH	1
	18R1, 45–54			0.21	1.59	4.30	8.90	3.80			Tr(583)	SH	1,9
	18R1, 118–120[c]	0.43	0.017	0.07	0.55	4.60	4.84		2.85	2.84		SH	1
	18R1, 78–80				0.04	10.00			2.99	2.99		SH	8
	18R1, 108–113			0.05	0.61	4.30	8.43	3.60				SH	9
	18R1, 123–125				0.20				2.89	2.89			8
	18R2, 6–9[c]	0.05	0.004	0.09	0.32	22.50	39.38	13.20	2.75	2.74		SH	1
	18R2, 61–63[c]	0.35	0.002	0.10	0.26	32.10	50.40	27.20	2.66	2.65		SH	1
	18R2, 80–85[c]	1.34	0.030	0.10	1.00	5.00	9.45	4.40	2.79	2.76		SH	1,9
	18R2, 90–92				0.18				2.84	2.83		SH	8
670	1D1, 19–21	4.01	0.045									SH	5
	2D1, 45–47	1.99	0.027									SH	5
	3W1, 12–14[c]	4.25	0.038	0.86	3.60	17.80	35.60	22.60	2.71	2.61		SH	4,5,6
	4W1, 19–21	0.23	0.005						2.79			SH	5
	5R1, 11–13	0.11	0.005			17.00	30.26					SH	7.6
	5R1, 12–14	0.11	0.005									SH	6
	5R1, 37–39[c]	3.41	0.136	0.32	5.30	5.10	14.79	6.80				SD	4
	5R1, 52–54	2.47	0.100	0.20	2.99	5.50	14.03				Tirr(580)	SD	7.6
	5R1, 55–57	11.98	0.115	0.39	5.60	5.30	15.37	3.25				SD	4,6
	5R1, 56–	0.51	0.094									SD	6
	5R1, 104–107[c]	1.73	0.072	0.10	2.50	4.50	13.05	8.80			Tirr(580)	SD	4
	5R1, 111–113	3.70	0.110	0.16	2.87	5.50	15.84	4.20	2.76	2.68		SD	7,6,5
	5R1, 114–116[c]	2.53	0.109	0.32	6.40	5.00	17.00	6.50				SD	4,6
	5R1, 126–128	8.26	0.111	0.20	2.93	5.50	14.80	3.00	2.65	2.57		SD	7,5,6
	5R1, 131–133[c]	3.12	0.083									SD	6
	5R1, 134–136[c]	2.08	0.103	0.44	7.40	6.10	17.69	8.60			Tr(580)	SD	4,6
	5R2, 5–7[c]	1.39	0.134	0.22	5.40	4.80	18.24	7.80			Tr(580)	SD	4
	5R2, 19–21[c]	6.70	0.108										6
	5R2, 22–24	3.35	0.153	0.26	4.58	5.30	15.48					SD	7,6
	5R2, 32–34[c]	6.28	0.035	0.23	2.30	9.50	27.55	3.70			Tr(580)	SD	4
	5R2, 52–54	1.33	0.056	0.12	1.59	6.00	14.22	7.00	2.71	2.66		SD	7,5,6
	5R2, 55–57[c]	2.47	0.137	0.28	5.50	5.00	16.00	5.70			Tr(580)	SD	4,6
	5R2, 102–104[c]	0.49	0.011	0.11	0.60	12.80	26.88	17.50			Tirr(580)	SH	4,6
	5R2, 109–111[c]	0.33	0.006										6
	5R2, 123–	0.35	0.006										6
	5R2, 134–136	0.27	0.007	0.06	0.26	14.20	25.70					SH	7,6
	6R1, 4–6[c]	0.07	0.004	0.04	0.20	10.70	22.47	8.50	2.80	2.80		SH	4,5,6
	6R1, 30–34	0.61	0.011	0.06	0.40	12.20	26.84	7.10			Tirr(580)	SH	4
	6R1, 37–39	0.19	0.008	0.06	0.29	13.80	25.53				Tirr(580)	SH	7,6
	7R1, 42–43[c]	3.52	0.096	0.19	4.80	5.30	19.08	7.40				SD	4
	7R1, 43–45	7.20	0.107	0.19	3.17	6.10	18.48	4.00	2.66	2.57		SD	7,6
	7R1, 73–75	1.40	0.062	0.26	1.92	10.20	20.81				Tirr(580)	SD	7,6
	7R1, 100–	6.09	0.085										6
	8R1, 31–34[c]	0.59	0.015	0.11	0.70	12.00	26.40	10.60				SH	4,6
	9R1, 12–14[c]	3.71	0.121	0.59	5.90	8.80	21.12	7.30				SH	4
920B	1W1, 55–57	7.72	0.053						2.68			SH	3
	1W 2, 24–26	15.10	0.086						2.72			SH	3
	1W 2, 95–97	18.04	0.072						2.78			SH	3
	1W 3, 46–48[c]	17.03	0.100	1.01	5.06	13.00	18.72	10.40	2.74	2.59		SH	1
920B	2R 1, 17–19	14.75	0.093						2.74			SH	3
	3R 2,36–38	18.82	0.091						2.74			SL	3
	3R 2, 98–100	13.36	0.077						2.71			SL	3
	4R 1, 60–62	8.76	0.087						2.74			SH	3
	5R 1, 52–54	15.10	0.083						2.71			SH	3
	5R 2, 60–62	15.76	0.087						2.74			SH	3
	5R 3, 61–63	23.00	0.075						2.71			SL	3

Table 1. (continued)

Hole	Sample	NRM, A/m	*K*, SI	Jrs, A m^2/kg	Js, A m^2/kg	Hc, mT	Hcr, mT	MDF, mT	*d*, g/cm^3	d_c, g/cm^3	*T*°C, °C	Lith	Ref[b]
	5R 3, 99–101	11.43	0.060						2.71			SL	3
	6R 3, 20–22	9.39	0.077						2.77			SH	3
	6R 3, 23–25	8.02	0.062						2.74			SH	3
	6R 3, 57–59	3.31	0.029						2.89			SH	3
	7R 2, 42–44[c]	38.44	0.108	0.65	4.32	8.51	13.62	8.20	2.72	2.60		SH	1
	8R 2, 24–26	11.58	0.101						2.70			SH	3
	8R 2, 70–72	10.21	0.119						2.72			SH	3
	8R 2, 73–75	8.33	0.109						2.73			SH	3
	8R 3, 69–71	8.66	0.105						2.71			SH	3
	8R 3, 115–117	9.52	0.100						2.73			SH	3
	8R 3, 118–120	9.15	0.101						2.80			SH	3
	8R 4, 11–13	6.73	0.095						2.70			SH	3
	8R 5, 62–64	9.82	0.093						2.72			SH	3
	9R 1, 41–43	17.08	0.105						2.75			SH	3
	9R 2, 36–38	15.57	0.110						2.74			SH	3
	9R 2, 39–41	15.01	0.100						2.71			SH	3
	9R 2, 84–86	14.78	0.086						2.71			SH	3
	9R 2, 87–89	14.28	0.083						2.71			SH	3
	10R1, 20–22	12.99	0.090						2.74			SH	3
	10R 2, 2–4	6.52	0.078						2.72			SH	3
	10R 2, 70–72	11.54	0.082						2.73			SH	3
	10R 3, 120–122	6.95	0.079						2.83			SH	3
	10R 4, 64–66	7.13	0.085						2.74			SH	3
	10R 5, 13–15	7.54	0.098						2.75			SH	3
	11R 1, 70–72	9.27	0.051						2.75			SH	3
	11R 1, 119–121[c]	15.88	0.069						2.76			SH	3
	11R 2, 10–12	11.73	0.075						2.79			SH	3
	12R 1, 51–53	7.26	0.073						2.82			SH	3
	12R 1,100–102	10.00	0.086						2.72			SH	3
	12R 2, 50–52	10.48	0.072						2.76			SH	3
	12R 3, 80–82	9.74	0.075						2.73			SH	3
	12R 4, 80–82[c]	10.35	0.096						2.72			SH	3
	12R 5, 10–12	8.45	0.083						2.74			SH	3
	12R 6, 16–18	11.46	0.087						2.72			SH	3
	13R 1, 60–62	20.33	0.085						2.77			SL	3
	13R 1, 94–96	18.94	0.085	0.59	3.70	10.20	13.06	9.00	2.74	2.64		SL	1
	13R 2, 80–82	15.98	0.082						2.65			SH	3
	13R 3, 36–381	15.88	0.082						2.86			SH	3
920D	2R1, 21–23	16.23	0.081						2.73			SH	3
	3R, 2 49–51[c]	24.73	0.100						2.70			SH	3
	4R 1, 22–24[c]	12.64	0.101	0.69	4.62	10.50	11.03	8.80	2.71	2.58		SH	1
	4R 2, 17–19	11.04	0.100						2.70			SH	3
	4R 3, 35–37	10.75	0.087						2.69			SH	3
	5R 2, 33–35	14.65	0.093						2.72			SH	3
	5R 3, 127–129	16.26	0.082						2.70			SH	3
	5R 4, 93–95	15.10	0.096						2.72			SH	3
	6R 1, 53–55	11.30	0.094						2.73			SH	3
	6R 2, 48–50	9.03	0.078						2.71			SH	3
	6R 3, 54–56	13.33	0.086						2.70			SH	3
	8R 1, 141–143	12.07	0.092						2.70			SH	3
	8R 2, 43–45	7.08	0.070						2.73			SH	3
	10R 2, 134–136	9.45	0.110						2.74			SH	3
	10R 3, 77–79	12.08	0.090						2.72			SH	3
	10R 4, 80–82	12.94	0.092						2.74			SH	3
	11R 1, 27–29	20.27	0.129						2.77			SD	3
920D	11R 1, 125–127	16.00	0.085						2.70			SH	3
	11R 1, 133–135[c]	14.18	0.094	0.89	4.23	11.40	14.59	8.80	2.62	2.50	Tr(583)	SH	1
	11R 2, 66–68	18.10	0.097						2.72			SH	3
	11R 3, 22–24	15.64	0.089						2.70			SH	3
	12R 1, 104–106	12.99	0.080						2.71			SH	3
	12R 2, 122–124	11.83	0.103						2.73			SH	3
	12R 3, 86–88[c]	6.91	0.055						2.73			SH	3
	12R 4, 54–56	9.07	0.088						2.77			SH	3
	12R 5, 23–25	9.80	0.071						2.68			SH	3
	13R 2, 84–86	10.38	0.066						2.82			SH	3
	13R 3, 126–128[c]	5.57	0.042	0.45	2.35	11.80	19.12	11.00	2.71	2.64		SH	1
	13R 4, 41–43	6.30	0.056						2.79			SH	3
	14R 1, 58–60	10.84	0.090						2.72			SH	3
	14R 3, 82–84	5.50	0.051						2.81			SH	3
	14R 4, 137–139	9.17	0.078						2.75			SH	3
	14R 5, 69–71[c]	11.23	0.091	0.70	5.37	8.68	15.71	8.80	2.73	2.58		SH	1

Table 1. (continued)

Hole	Sample	NRM, A/m	*K*, SI	Jrs, A m^2/kg	Js, A m^2/kg	Hc, mT	Hcr, mT	MDF, mT	*d*, g/cm^3	d_c, g/cm^3	*T*°C, °C	Lith	Ref[b]
	15R 1, 80–82	9.98	0.074						2.75			SH	3
	15R 2, 92–94	15.54	0.078						2.73			SH	3
	15R 3, 48–50	12.14	0.067						2.77			SH	3
	16R 1, 98–101[c]	9.05	0.088						2.77			SH	3
	16R 3, 5–7	5.54	0.059						2.75			SH	3
	16R 4, 82–84	9.87	0.092						2.70			SH	3
	16R 5, 80–82	9.01	0.077						2.72			SH	3
	16R 7, 54–56	10.58	0.099						2.74			SH	3
	17R 3, 37–391	14.22	0.088						2.71			SH	3
	18R 1, 123–125	7.45	0.075						2.71			SH	3
	18R 3, 75–77	14.78	0.126						2.80			SD	3
	18R 4, 12–14	12.06	0.077						2.72			SD	3
	19R 1, 18–20	5.26	0.065						2.67			SD	3
	19R 2, 13–15	14.76	0.099						2.76			SD	3
	20R 1, 106–108	11.28	0.086						2.74			SH	3
	20R 2, 24–26	10.11	0.075						2.78			SH	3
	20R 4, 38–40	9.48	0.078						2.75			SH	3
	21R 1, 93–95[c]	10.90	0.073						2.78			SH	3
	21R 1, 103–105[c]	13.47	0.077	0.74	3.52	12.20	17.08	12.80	2.65	2.55		SH	1
	21R 2, 40–42	9.76	0.068						2.79			SH	3
	21R 2, 97–99	13.07	0.085						2.73			SH	3
	22R 4, 50–52	5.16	0.047						2.84			SH	3
	22R 5, 104–106[c]	5.11	0.050						2.73			SH	3
895B	1R1, 54–56	0.63	0.007	0.04	0.17	14.15	25.47					SH	10
	1R1, 64–66	0.47	0.007					12.00	2.75			SH	11
895C	3R1, 5–7	0.99	0.029	0.29	0.78	29.50	44.25				Tr(570)	SH	10
	3R1, 139–141	2.03	0.023					15.00	2.72			SH	11
	3R2, 19–21	2.07	0.043	0.26	2.36	9.02	20.75	10.90			Tr(582)	SH	10
	4R1, 23–25	1.22	0.015	0.19	0.86	17.78	32.00					SH	10
	4R2, 105–107	2.11	0.020	0.23	0.80	19.22	30.75					SD	10
895D	2R1, 25–27	0.45	0.006	0.09	0.38	17.30	27.68	19.20			Tr(585)	SH	10
	2R1, 47–49	1.02	0.010					14.00	2.76			SH	11
	2R2, 22–24	2.16	0.033	0.30	1.24	18.94	34.09					SH	10
	2R2, 25–27			0.62	2.21	21.03	35.75					SH	10
	2R2, 39–41	0.81	0.026	0.13	0.90	10.02	19.04					SH	10
	2R2, 47–49	1.35	0.037					7.00	2.69			SH	11
	3R1, 30–32			0.02	0.14	11.14	23.39					SH	10
	3R1, 45–47	0.26	0.006					12.50	2.76			SH	11
	4R1, 41–43	0.57	0.004	0.03	0.17	13.49	25.63	14.90				SH	10
	4R2, 39–41			0.04	0.25	15.46	30.92					SH	10
	4R2, 123–125	1.01	0.015	0.07	0.56	10.90	22.89					SH	10
	4R3, 4–6	1.07	0.011	0.09	0.80	9.09	20.18	19.30				SH	10
	4R3, 72–74	0.38	0.003	0.02	0.11	13.56	27.12					SH	10
	4R3, 110–112	0.43	0.004					15.00	2.84			SH	11
	4R4, 19–21[c]	0.54	0.003	0.02	0.11	17.60	31.68					SH	10
	4R4, 100–102	0.69	0.008	0.05	0.26	14.40	25.92	17.10				SH	10
895D	4R5, 3–5	0.61	0.005					20.00	2.86			SH	11
	4R5, 8–10	0.52	0.004	0.02	0.10	17.35	31.23					SH	10
	5R1, 52–54	1.48	0.025					12.00	2.80			SH	11
	5R2, 100–102	0.78	0.012					15.00	2.71			SH	10
	6R1, 75–77	3.25	0.034	0.26	0.90	16.41	26.26					SH	10
	6R1, 99–101	1.92	0.032	0.45	1.99	17.74	30.16	17.80			Tr(579)	SH	10
	7R1, 119–12	0.39	0.028					12.00	2.68			SH	11
	7R2, 92–94[c]	2.04	0.033					12.00	2.57			SH	11
	7R2, 107–109	0.96	0.021	0.23	1.32	12.46	23.67	13.70			Tr(582)	SH	10
	8R1, 45–47	3.21	0.028					10.00	2.64			SD	11
	8R2, 119–121			0.22	2.81	7.77	20.20					SD	10
	9R1, 78–80	2.47	0.045	0.43	2.51	12.32	20.94	13.60			Tr(584)	SD	10
	9R1, 120–122	25.04	0.067					18.00	2.58			SD	11
	9R1, 129–131	9.97	0.060	0.30	1.69	10.80	20.52					SD	10
	9R1, 140–142			0.27	3.15	7.90	20.54				Tr(580)	SD	10
895E	1R2, 72–74	5.06	0.075					10.00	2.57			SD	11
	1R2, 105–107	4.99	0.069	0.45	3.21	10.48	19.91	14.80			Tr(582)	SD	10
	1R2, 129–131	5.99	0.081	0.31	3.12	7.86	16.51				Tr(579)	SD	10
	1R3, 24–26	3.82	0.060	0.31	1.84	12.15	21.87					SD	10
													10,1
	1R3, 49–51	5.34	0.114	0.57	4.03	10.17	20.34	10.00	2.60	2.48		SH	1
	1R3, 86–88	3.45	0.075	0.36	2.72	10.37	19.70	10.60				SH	10
	2R2, 56–58	12.99	0.077	0.46	2.53	10.81	20.54					SD	10
	2R2, 107–109	7.58	0.060					13.00	2.56			SD	11
	3R1, 90–92	1.55	0.033	0.21	1.37	11.11	21.11				Tr(579)	SH	10

Table 1. (continued)

Hole	Sample	NRM, A/m	*K*, SI	Jrs, A m^2/kg	Js, A m^2/kg	Hc, mT	Hcr, mT	MDF, mT	*d*, g/cm^3	d_c, g/cm^3	*T*°C, °C	Lith	Ref[b]
	3R–2, 24–26	8.80	0.079	0.35	2.36	8.71	17.42					SD	10
	3R2, 55–57	10.34	0.115					10.00	2.59			SD	11
	3R–2, 136–138			0.71	4.65	9.20	19.32				Tr(579)	SD	10
	3R3, 14–16[c]	4.67	0.125	0.44	4.39	8.93	19.65	9.00	2.60			SD	10,1
	4R1, 92–94	3.33	0.046	0.27	2.51	8.60	18.06	8.20				SD	10
	4R1, 102–104	3.21	0.058					7.00	2.60			SD	11
	4R2, 58–60	3.93	0.052	0.25	1.32	12.49	23.73					SD	10
	5R1, 112–114	3.04	0.061	0.52	2.75	16.20	27.54	11.70				SD	10
	5RI, 145–147	4.35	0.068					9.00	2.60			SD	11
	5R2, 48–50	3.45	0.052	0.39	2.55	12.30	23.37	15.40			Tr(578)	SD	10
	5R2, 115–11	4.78	0.076	0.27	2.07	11.47	24.09	7.00	2.60	2.54		SD	10,1
	6R1, 131–133	3.38	0.049	0.22	1.36	11.21	22.42					SD	10
	6R2, 85–87	1.71	0.045	0.27	2.10	11.57	24.30	10.70				SD	10
	6R2, 111–113[c]	2.30	0.027	0.14	0.87	12.18	24.36	14.00	2.61	2.59		SD	10,1
	6R3, 17–21	4.53	0.023	0.23	1.36	12.31	23.39	4.40				SD	10
	6R3, 101–103	1.93	0.026					7.00	2.62			SD	11
	6R5, 66–68	5.25	0.047					7.00	2.60			SD	11
	6R5, 74–76	1.88	0.047	0.19	1.61	8.79	18.46	12.70				SD	10
	7R1, 113–115[c]	5.28	0.069	0.71	4.43	12.30	22.14	10.30				SD	10
	7R1, 135–137	4.58	0.059	0.34	2.64	10.10	20.20	9.30			Tr(581)	SD	10
	7R2, 102–104	2.79	0.046					12.00	2.61			SD	11
	7R3, 60–62	2.12	0.036					10.00	2.63			SD	11
	7R3, 86–88	1.94	0.040	0.23	1.72	11.49	22.98					SD	10
	7R3, 125–127	3.19	0.062	0.24	2.41	9.26	19.45					SD	10
	7R3, 145–147[c]	1.48	0.024	0.22	1.00	17.83	30.31	24.00				SD	10
	7R4, 36–38	1.04	0.013	0.12	0.62	15.18	25.81	11.00	2.68	2.66		SH	10,1
	8R1, 99–101	2.98	0.046	0.20	1.82	9.62	24.05	22.00				SD	10
	8R1, 113–115	2.49	0.045	0.23	1.58	11.46	21.77	22.50				SD	10
	8R2, 57–59	3.72	0.059	0.38	2.72	11.04	22.08	7.00	2.59	2.51		SH	10,1
	8R2, 70–72	2.48	0.037	0.25	1.86	10.80	20.52	9.50			Tr(575)	SH	10
	8R2, 100–102	2.00	0.066	0.21	3.00	7.03	21.79	8.30				SH	10
	8R3, 66–68	1.46	0.070	0.25	1.91	10.23	21.48					SD	10
	8R3, 114–116	3.28	0.046	0.29	1.84	12.59	23.92					SD	10
895 F	2R1, 21–23	2.59	0.026	0.31	1.93	13.17	23.71	13.90				SH	10
	2R1, 92–94	3.96	0.038	0.22	1.30	12.21	21.98					SH	10

[a] NRM, natural remanent magnetization; *K*, magnetic susceptibility; Jrs, saturation remanent magnetization; Js, saturation magnetization; Hc, coercive force; Hcr, remanent coercive force; MDF, median destructive field; *d*, grain density; *T*°C, Curie temperature (Tirr, irreversible thermomagnetic curve, and Tr, reversible thermomagnetic curve); Lith, lithology (HS, serpentinized harzburgite; SD, serpentinized dunite; SL, serpentinized lherzolite).

[b] References: 1, this study; 2, *Smith and Banerjee* [1985]; 3, *Cannat et al.* [1995]; 4, *Bina and Henry* [1990]; 5, *Detrick et al.* [1988]; 6, *Hamano et al.* [1990]; 7, *Krammer* [1990]; 8, *Johnson* [1979]; 9, *Dunlop and Prévot* [1982]; 10, *Kelso et al.* [1996]; and 11, *Mével et al.* [1993].

[c] Samples for which a thin section is available.

ago at the East Pacific Rise, then rifted at the tip of the Cocos-Nazca propagating ridge (Hess Deep).

[13] Serpentinized peridotites at all these sites have been drilled either directly at the seafloor (sites <1 Myr old: ODP sites 670, 895, and 920) or under a few meters to a few hundred meters of sediments and basalt (DSDP sites 395, 556, 558, and 560). Their petrographic characteristics indicate that they are derived from variably depleted mantle peridotites [*Arai and Fujii*, 1978; *Michael and Bonatti*, 1985; *Ghose et al.*, 1996; *Dick and Natland*, 1996]. Exposure of these deeply derived rocks at or near the seafloor is attributed to large offset normal faulting of the oceanic lithosphere, as a result of slow spreading ridge tectonics in the case of the MAR samples [e.g., *Tucholke and Lin*, 1994; *Cannat et al.*, 1997], and due to rifting of a preexisting oceanic crust in the case of the Hess Deep samples [*Francheteau et al.*, 1990; *Karson et al.*, 1992].

3.2. Description of Drilled Serpentinized Peridotite Intervals

[14] Although they have been drilled significant distances apart, DSDP sites 556, 558, and 560 have similar lithostratigraphies: ~400 m of sediments, then a sequence of pillowed and brecciated basalts (<1-m to 120-m-thick) overlying extensively brecciated serpentinized peridotites and gabbros [*Bougault et al.*, 1985]. Detailed examination of the core at the Lamont-Doherty repository confirms the cataclastic origin of this breccia, which probably formed in a fault zone. Peridotites from these sites are extensively serpentinized (>90%) and have a reddish color indicative of significant oxidation [*Bougault et al.*, 1985]. The 11 samples listed in Table 1 are representative of the least cataclastically deformed portions of the core at the three sites.

[15] Serpentinized peridotites drilled at DSDP site 395 also belong to a breccia, but the origin of this breccia is detritic (rounded to angular pebbles in a matrix of consolidated ooze [*Melson et al.*, 1976]. This ultramafic breccia occurs in 2-m-thick intervals, intercalated within a sequence of pillow basalts. This basaltic sequence is overlain by 90 m of sediments. Peridotites from this site are moderately to extensively serpentinized (50–100%) harzburgites [*Melson et al.*, 1976] and generally have a reddish color indicative of oxidative alteration. The oxygen isotope composition of serpentine in one moderately serpentinized sample and in extensively serpentinized ones suggests that serpentinization occurred at higher temperature in less serpentinized intervals (~380°C against ~280°C in the extensively serpentinized sample [*Hornes et al.*, 1978]). The 12 samples listed in Table 1 are representative of the various degrees of serpentinization observed at this site.

[16] ODP site 670 was drilled directly into serpentinites, with low recovery rates (7% on average for a 93-m-deep hole [*Detrick et al.*, 1988]). Serpentinization at this site varies between 40% and

100% [*Komor et al.*, 1990; *Hébert et al.*, 1990]. Intervals of moderately serpentinized peridotites commonly have a reddish color indicating late oxidation. Oxygen isotopic compositions of serpentine-magnetite pairs in these intervals correspond to relatively low serpentinization temperatures (<200°C [*Hébert et al.*, 1990; *Komor et al.*, 1990; *Agrinier and Cannat*, 1997]). By contrast, extensively serpentinized intervals are dark green, and oxygen isotopic compositions of serpentine-magnetite pairs are typical of high-temperature serpentinization (>350°C [*Agrinier and Cannat*, 1997]). One interval of dark green, 100% serpentinized peridotite (46–52 m below seafloor) has a peculiar, "tortoise shell" texture [*Detrick et al.*, 1988], characterized by widely spaced crosscutting serpentine veins and by the absence of bastites (serpentine pseudomorphs after pyroxene). The 35 samples listed in Table 1 are representative of the various degrees of serpentinization observed at this site, with a large representation (16 samples) of the tortoise shell textured interval.

[17] ODP site 920 was also drilled directly into serpentinites, 18 km to the north of site 670. Good recovery (40% on average for two holes, one 100 m deep and the other 200 m deep) allows for a reliable assessment of the lithostratigraphy at this site. It consists in a homogeneous sequence of dark green serpentinized harzburgite (degree of serpentinization: 70–100%), with thin gabbroic dikelets [*Cannat et al.*, 1995]. Oxygen isotope geothermometry indicates high temperatures of serpentinization (>350°C [*Agrinier and Cannat*, 1997]). The 105 samples listed in Table 1 are representative of the two holes drilled at site 920 and range in depth of provenance between 0.6 and 199 m below seafloor.

[18] Finally, ODP site 895 was drilled directly into serpentinized peridotites near the top of the Hess Deep "intrarift ridge" [*Mével et al.*, 1993]. Recovery was mediocre (21% on average for a 93-m-deep hole). The drilled sequence comprises serpentinized dark green harzburgite (degree of serpentinization: 50–100%) and serpentinized dark green dunite (degree of serpentinization: 80–100%), with intervals of troctolite and gabbro [*Mével et al.*, 1993]. Oxygen isotope geothermometry indicates high temperatures of serpentinization (>350°C [*Früh-Green et al.*, 1996; *Agrinier et al.*, 1996]). The 82 samples listed in Table 1 are representative of the range of lithologies and degrees of serpentinization observed at the site and range in depth of provenance between 16 and 79 m below seafloor.

3.3. Petrographic Description of Studied Samples

[19] Previously published and new magnetic data presented in this paper concern 245 samples (Table 1). We have studied 54 of these samples in thin sections (9 for sites 556, 558 and 560; 7 for site 395; 7 for site 670; 19 for site 920; and 12 for site 895; Table 1). Descriptions of textures associated with the primary mineralogy or with recrystallization of primary minerals in peridotites from the seven studied drill sites have been published as part of the DSDP and ODP Initial Report and Scientific Results volumes [*Michael and Bonatti*, 1985; *Arai and Fujii*, 1978; *Sinton*, 1978; *Komor et al.*, 1990; *Hébert et al.*, 1990; *Früh-Green et al.*, 1996; *Niida*, 1997]. In this section we focus on textures that are associated with serpentinization.

[20] Moderately serpentinized peridotites (<70%), when present, have similar textures at all sites: serpentine isolates rounded or elongated olivine relics and magnetite concentrates in a few crosscutting veins (Figure 2a); orthopyroxene, when present, is only marginally replaced by bastite; clinopyroxene, when present, is preserved; spinel is marginally replaced by magnetite and ferrichromite. Extensively serpentinized peridotites (>70%) display typical serpentine mesh textures [e.g., *Wicks and Whittaker*, 1977] replacing olivine-rich zones (Figure 2b), except in the tortoise shell textured interval at site 670. Serpentine mesh size varies between 0.5 and 1 mm. Mesh centers are made of apparently amorphous serpentine and contain little magnetite; mesh rims are commonly filled with fibrous serpentine and contain most of the magnetite. Pyroxenes are replaced by bastites that are commonly devoid of magnetite and grow preferentially near grain boundaries and fractures. Spinel cores are generally preserved. In most samples from site 895, mesh centers contain a brownish and pleochroic assemblage of brucite and serpentine (Figure 2c) [*Mével and Stamoudi*, 1996]. In some samples from site 920, mesh centers locally contain needle-shaped grains of Fe-Ni sulfides [*Dilek et al.*, 1997].

[21] Extensively serpentinized peridotites in the tortoise shell textured interval at site 670 do not contain bastites and have therefore been ascribed a dunitic protolith [*Hébert et al.*, 1990]. They also do not display the characteristic serpentine mesh texture: Apparently amorphous serpentine in these samples forms wide, magnetite-poor domains, while magnetite concentrates near thick serpentine veins (Figure 2d).

4. Magnetic Properties of Serpentinized Peridotites

4.1. Thermomagnetic Curves: Curie Temperature and Magnetic Mineralogy

[22] Thermomagnetic curves have been obtained for representative samples from the seven DSDP and ODP sites in order to characterize their magnetic mineralogy (see Table 1). For samples analyzed as part of the present study and by *Richter et al.* [1996], these curves have been obtained in a low field, using a Kappabridge instrument. For samples analyzed by *Bina and Henry* [1990]; *Krammer* [1990] and *Kelso et al.* [1996], thermomagnetic curves were acquired in a strong magnetic field.

[23] In most samples, thermomagnetic curves are reversible and correspond to Curie temperatures of ~580°C, indicating that magnetite is the principal carrier of magnetization. However, irreversible curves have been obtained in samples from sites 556, 558, and 560, showing a magnetization loss upon cooling [*Smith and Banerjee*, 1985; this study]. In these samples the heating portion of the thermomagnetic curve shows two inflection points: one at ~350°C and the other at ~580°C. This suggests that the observed magnetization loss is due to the replacement of a significant amount of maghemite by hematite while the sample was brought to temperatures above 350°C [e.g., *Krammer*, 1990]. A few samples from sites 395 and 670 show similarly irreversible curves, with a less pronounced inflection at ~350°C [*Krammer*, 1990; this study], suggesting a lesser abundance of maghemite. A few other samples from sites 395 and 670 have irreversible thermomagnetic curves that show an increase in magnetization upon cooling [*Dunlop and Prévot*, 1982; *Bina and Henry*, 1990; this study]. In some samples, this increase is small and may be due, as proposed by *Lienert and Wasilewski* [1979], to the transformation of nonstochiometric iron phases into magnetite. In other samples, however, this increase is large and remains unexplained [*Bina and Henry*, 1990].

4.2. Magnetic Susceptibility and Natural Remanent Magnetization

[24] Figure 3a shows low field magnetic susceptibility (K) and natural remanent magnetization (NRM) values for the 245 samples considered in our study (Table 1). NRM values in many samples compare with those of oceanic basalts, but corresponding K values are significantly higher. It is also remarkable that while there is a general tendency for NRM values to increase at increasing values of K, the rate of this increase differs from one drill site to another (Figure 3a).

[25] Most samples from site 395 have low magnetic susceptibility ($K < 0.02$ SI) and low NRM values. K is higher in many samples from sites 556, 558, and 560, but NRM values in these samples remain low (Figure 3a). This could be due to extensive low-temperature oxidation of magnetite in these samples [*Smith*, 1987]. Site 670 samples with K values greater than 0.05 SI have

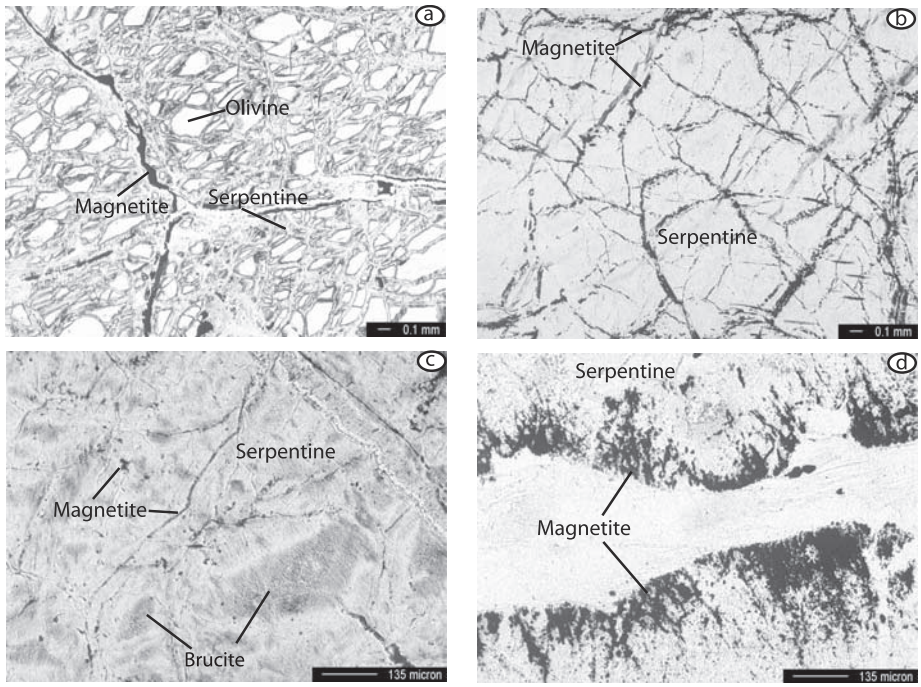

Figure 2. Photomicrographs (transmitted light) of partially and completely serpentinized peridotites. (a) Partially serpentinized peridotite with olivine relicts in a serpentine mesh. Magnetite concentrates in crosscutting serpentine veins (DSDP site 395, sample 18R1, 118–120 cm). (b) Completely serpentinized peridotite with typical serpentine mesh texture. Magnetite concentrates in serpentine veins that bound individual mesh cells (ODP hole 920B, sample 7R2, 45–48 cm). (c) Completely serpentinized peridotite from ODP site 895. The center of serpentine mesh cells is made of finely intergrown serpentine and brucite (ODP hole 895D, sample 7R2, 94–96 cm). (d) Completely serpentinized peridotite from ODP site 670. The typical serpentine mesh texture is absent. Magnetite concentrates near large serpentine veins (ODP site 670, sample 5R2, 55–57 cm).

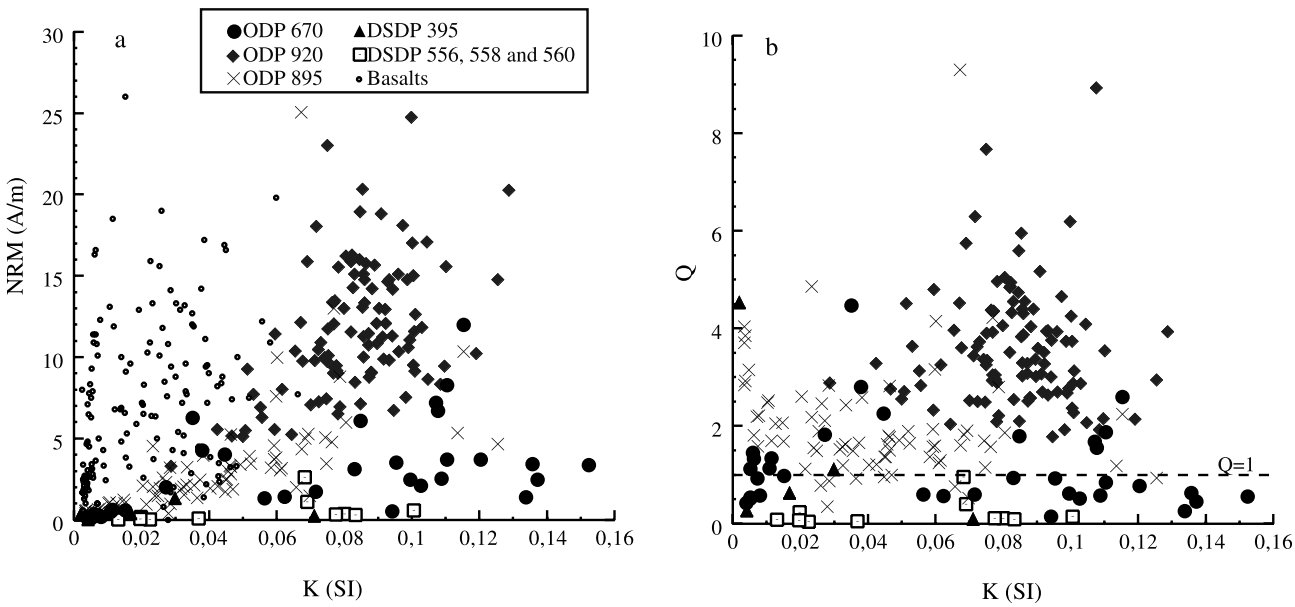

Figure 3. Natural remanent magnetization (NRM) and Koenigsberger ratio (Q) in 245 serpentinized peridotite samples, as a function of the low field magnetic susceptibility (K). Basalts values shown for comparison [*Day et al.*, 1979; *Bina et al.*, 1990].

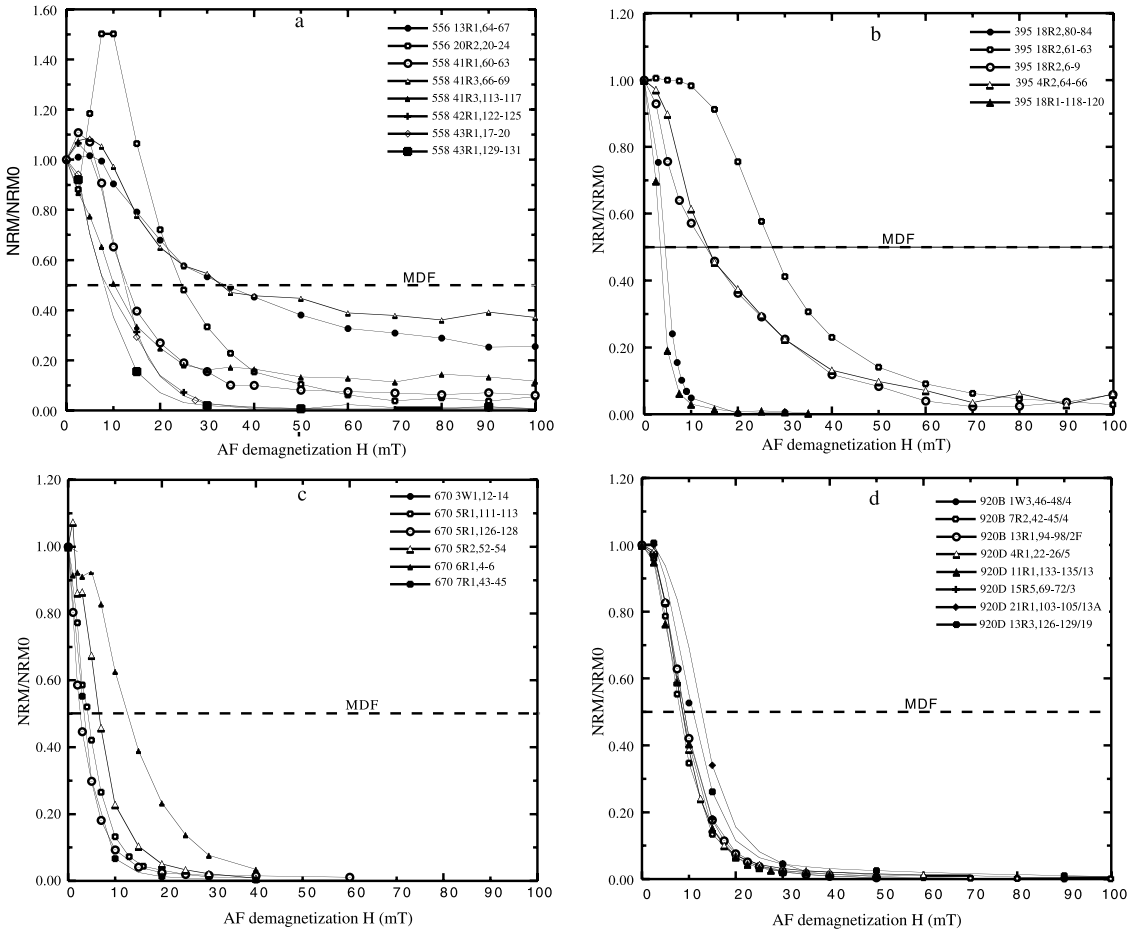

Figure 4. Normalized AF demagnetization curves for serpentinized peridotite samples. (a) DSDP sites 556, 558, and 560. (b) DSDP site 395. (c) ODP site 670 (M. Bina, unpublished data, 1990). (d) ODP site 920. Dashed lines intersect these curves at the value of the median destructive field (MDF) for each sample.

variable, mostly low (<4 A/m) NRM values that do not show a systematic increase at increasing *K*. A positive NRM versus *K* correlation does exist, although with great scatter, for high *K* samples of site 895 [*Kelso et al.*, 1996]. Finally, samples from site 920 have high (>4 A/m) NRM values. Most of these samples also have high *K* values (>0.07 SI) and show a large scatter of NRM values at any given value of *K* (Figure 3a). A few samples from sites 670 and 895 do plot within this scatter.

[26] The variability in NRM versus *K* trends translates into significant between sites variations of the ratio of remanent to induced magnetization (Koenigsberger ratio or *Q*). In Figure 3b we use a common value for the intensity of the geomagnetic field (50 μT ≈ 40A/m) and compare *Q* values at each site. *Q* is <1 in most samples from sites 395, 556, 558, 560, and in many samples from site 670. Induced magnetization is therefore dominant in these samples. *Q* is between 1 and 3 in most samples from site 895 (mean $Q = 2.02 \pm 1.24$) and in a few samples from site 670. *Q* is between 2 and 5 in most samples from site 920 (mean $Q = 3.6 \pm 1.2$). Remanent magnetization is therefore dominant in these samples. However, *Q* values even in these remanent serpentinized peridotites remain significantly lower than basaltic *Q* values (~20 [*Day et al.*, 1979; *Bina et al.*, 1990]).

4.3. Stability of NRM

[27] The remanence decay during alternating field (AF) demagnetization is shown in Figure 4 for 27 samples representative of sites 395, 556, 558, 560, 670 and 920. AF demagnetization data for site 895 samples can be found in the Initial Reports for leg 147. Most samples display two magnetic components [*Johnson*, 1978; *Smith and Banerjee*, 1985; *Bina and Henry*, 1990; *Hamano et al.*, 1990; *Kelso et al.*, 1996]: a soft component that may have been acquired during drilling and a hard component interpreted as the chemical remanent magnetization (CRM) acquired during serpentinization. Vector demagnetization diagrams are mainly unidirectional after removal of the soft component [e.g., see *Bina and Henry*, 1990, Figure 3]. The stability of the NRM can be estimated from the value of the median destructive field (MDF), which is the AF field required to demagnetize half of the NRM. MDF values in serpentinized peridotites vary between <5 mT (in some samples from sites 395 and 670; Figures 4b and 4c) and >30 mT (in extensively maghemitized samples from sites 556 and 558; Figure 4a). Average MDF values observed in serpentinized peridotite are ~10 mT, smaller than basalt values (~20 mT on average [*Day et al.*, 1979; *Bina et al.*, 1990]), indicating a lesser stability of the NRM carried by serpentinized peridotites. This is consistent with the dominantly concave shape of AF demagnetization curves, which indicates relatively large magnetic grain sizes [*Dunlop*, 1973; *Argyle et al.*, 1994].

4.4. Hysteresis Loop Parameters

[28] Hysteresis loop parameters (saturation magnetization Js, saturation remanent magnetization Jrs, coercivity Hc, and remanent coercivity Hcr) are listed in Table 1 for 115 samples (11 from sites

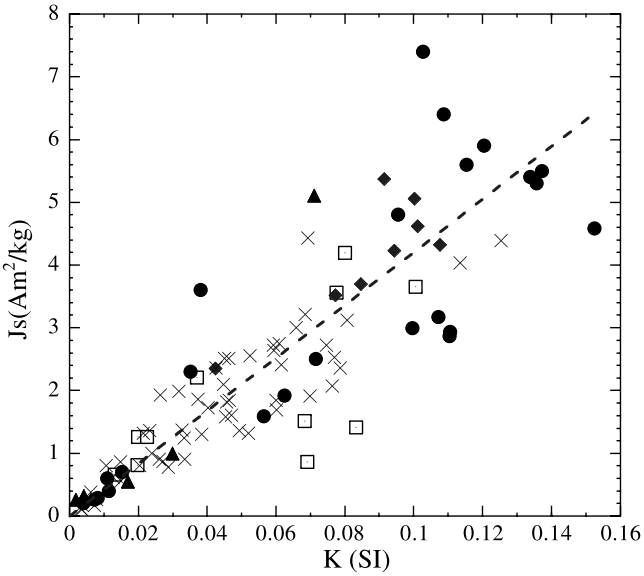

Figure 5. Saturation magnetization (Js) as a function of the low field magnetic susceptibility (K) in 115 serpentinized peridotite samples. Symbols are the same as in Figure 3. Dashed line shows best linear least squares fit (Js = 40.65K; R = 0.87).

556, 558, and 560, 12 from site 395, 24 from site 670, 8 from site 920, and 60 from site 895).

4.4.1. Saturation magnetization, magnetite content, and magnetic susceptibility. [29] Js values range from 0.04 to 7.4 A m^2/kg (Table 1) and can be used, assuming that magnetite is the only mineral that contributes to room temperature hysteresis, to calculate the magnetite volume fraction (m) in each sample (m = Js/Js of pure magnetite, 92 A m^2/kg). We have extended this calculation to samples that have been partially maghemitized because Js of pure maghemite is 74 A m^2/kg, not very different from that of magnetite. This calculated magnetite (or magnetite + maghemite) volume content (Table 1) varies between <1% (in many samples from sites 556, 558, 560, 395, 670, and 895) and >5% (in a few samples from sites 395, 670, and 920).

[30] Figure 5 shows that Js in abyssal serpentinized peridotite samples is linearly correlated with the low field magnetic susceptibility (K). The best fitting trend is linear and corresponds, for samples that are not maghemitized, to an equally linear empirical relation between K and the calculated magnetite content (K = 0.0224*m). This last relation is consistent with that predicted by ferrimagnetic theory for serpentinized peridotites containing randomly oriented multidomain (MD) magnetite particles [*Toft et al.*, 1990]. K in assemblages of true MD particles is expected to be proportional to the amount of magnetite mineral and independent of particle size [e.g., *Stacey and Banerjee*, 1974]. K in single-domain (SD) assemblages is, by contrast, expected to have a weak dependence on particle size [*Wohlfarth*, 1958; *Dunlop*, 1969; *Heider et al.*, 1996].

4.4.2. Magnetic grain size. [31] Jrs, Hc, and Hcr are directly related to the magnetic domain structure of magnetic particles. Ferromagnetic particles small enough to sustain an equilibrium single-domain (SD) magnetic structure have large remanences and coercive forces [see *Dunlop and Özdemir*, 1997]. Theoretical and experimental size limits for equidimensional SD magnetites are ~0.05–0.08 μm [*Dunlop*, 1973; *Butler and Banerjee*, 1975]. Truly multidomain (MD) behavior, characterized by low remanences and coercivity [e.g., *Dunlop and Özdemir*, 1997], is found experimentally in magnetite grains larger than ~3 μm [*Worm and Markert*, 1987] or than ~10–15 μm [*Stacey*, 1962; *Day et al.*, 1977; *Dunlop*, 1981]. In the broad size range between true SD and true MD behavior, magnetic properties have been shown to change gradually from SD-like at the smaller sizes to MD-like at the larger sizes [*Day et al.*, 1977; *Dunlop*, 1981]. This transitional behavior has been called pseudo-single-domain (PSD) behavior. The mechanisms of PSD behavior are not yet fully understood (see discussion by *Dunlop* [1981] and *Argyle and Dunlop* [1990]).

[32] The hysteresis parameters Jrs/Js (ratio of saturation remanence to saturation magnetization) and Hcr/Hc have diagnostic value to determine the domain structure of a magnetic sample. Magnetic theory predicts Jrs/Js > 0.5 and Hcr/Hc ≈ 1 for SD magnetites and Jrs/Js < 0.05 and Hcr/Hc > 4 for truly MD magnetites [*Stoner and Wohlfarth*, 1948; *Rahman et al.*, 1973; *Day et al.*, 1977; *Dunlop*, 1981]. Figure 6a shows that the serpentinized peridotites considered in this paper plot in the PSD region, at generally lower Jrs/Js and higher Hcr/Hc values than young oceanic basalts. It should be noted, however, that hysteresis parameters cannot distinguish true PSD magnetites from mixtures of MD and SD magnetites. We will subsequently use the term "effective magnetic grain size" to refer to the position of our samples with respect to the SD, PSD, and MD domains defined in Jrs/Js versus Hcr/Hc diagrams.

[33] Experimental data in the PSD range show that Jrs/Js, Hc, and Hcr decrease at increasing particles sizes (d). Best fitting functions for experimental data on crushed magnetites are power law functions in $d^{-0.4}$ to $d^{-0.5}$ for Jrs/Js and Hc and in $d^{-0.2}$ for Hcr [*Parry*, 1965; *Rahman et al.*, 1973; *Day et al.*, 1977; *Heider et al.*, 1987]. Figure 6b shows a linear correlation between Jrs/Js and Hc in our samples (most pronounced in samples from sites 670 and 895), consistent with experimental evidence that these two parameters are proportional to similar power law functions of d. The best fitting linear trend for our sample set, however, is distinct from the trend determined experimentally by *Day et al.* [1977]: most serpentinized abyssal peridotites have lower coercive forces at a given value of Jrs/Js than the crushed, then annealed synthetic aggregates of magnetite studied by *Day et al.* [1977]. Adhering fine particles and residual stresses from grinding in the synthetic aggregates are the likely causes for this discrepancy [*Dunlop*, 1986]. Only those samples that are extensively maghemitized (sites 556, 558 and 560) plot near the *Day et al.* [1977] curve in Figure 6b.

[34] Many samples from site 670 have low (~0.05) Jrs/Js, Hc, and Hcr values and high Hcr/Hc values, indicative of relatively coarse magnetic grain sizes. Some of these samples actually plot near the true MD region shown in Figure 6a. By contrast, samples from sites 895 and 920 generally have high Jrs/Js, Hc, and Hcr values, indicating more stable magnetization and smaller magnetic grain sizes. This contrast is enhanced in Figure 6c, which shows only those samples with K > 0.04 SI. It is consistent with samples from sites 895 and 920 having generally higher NRM, at a given value of K, than samples from site 670 (Figure 3). Most high K samples from site 920 have lower Hcr/Hc values than high K samples from site 895 (Figure 6c), suggesting smaller magnetic grain sizes. Most samples from sites 395, 556, 558, and 560 plot to the left of the Jrs/Js versus Hcr/Hc trend in Figure 6a. This is due to significantly higher Hc values (Figure 6b), probably caused by maghemitization [*Smith*, 1987].

4.4.3. Magnetic grain size and magnetite content. [35] Figure 7 shows the effect of variations in magnetite content (calculated from Js) of samples that are not maghemitized, on the magnetic grain size indicator Jrs/Js. Samples from site 895 have similar Jrs/Js but generally contain less magnetite than samples from site 920. It is therefore likely that the contrasting NRM values of serpentinized peridotites from these two sites (Figure 3) are primarily due to differences in magnetite content. Figure 7 shows no systematic variation of Jrs/Js with magnetite content in samples from sites 895 and 920. This indicates that there is no systematic relation at these two sites between effective magnetic grain size and magnetite content. By contrast, samples from site 670 show a trend of decreasing Jrs/Js at increasing magnetite contents,

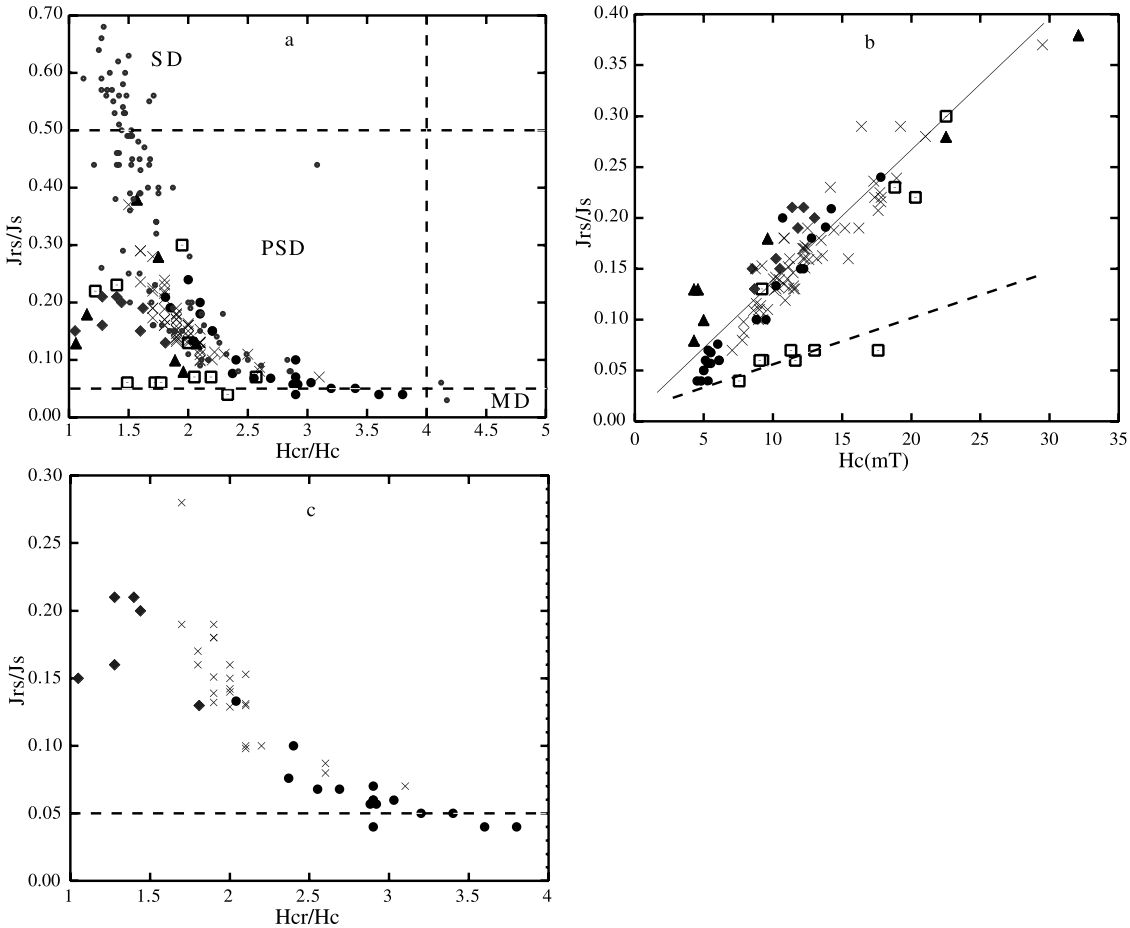

Figure 6. Hysteresis parameters Jrs (saturation remanent magnetization) and Js (saturation magnetization) as a function of Hcr (remanent coercitivity) and Hc (coercitivity) in serpentinized peridotites and oceanic basalts (small dots [*Day et al.*, 1979; *Bina et al.*, 1990]). Symbols are the same as in Figure 3. (a) Jrs/Js as a function of Hcr/Hc in 115 serpentinized peridotites samples. SD, single domain; PSD, pseudo-single domain; MD, multidomain (see text). (b) Jrs/Js as a function of Hc. Solid line, best linear least squares fit for the abyssal peridotite data set (Jrs/Js = 0.007 Hc + 0.012; R = 0.87). Dashed line, best fit for the magnetite aggregates studied by *Day et al.* [1977] (Jrs/Js = 0.0077Hc - 0.014). (c) Jrs/Js as a function of Hcr/Hc in a subset of serpentinized peridotites from ODP sites 670, 920, and 895, with magnetic susceptibilities (K) > 0.04 SI.

suggesting that the effective magnetic grain size at this site increases at increasing magnetite content. This evolution occurs in samples with <3% modal magnetite, i.e., samples with low Js (<3 A m^2/kg) and K values (<0.04 SI; Figure 5).

4.5. Magnetic Properties and Degree of Serpentinization

[36] The degree of serpentinization of a peridotite can be determined directly from modal analysis. The drawback of this direct method (besides being time consuming) is that it concerns thin sections, which may not be representative of the volume of sample used in measurements of magnetic properties. Because the densities of fresh olivine (~3.337 g/cm^3 for Fo_{90}) and orthopyroxenes (~3.285 g/cm^3 for En_{90}) are significantly larger than the density of serpentine (~2.550 g/cm^3), density can be used as a proxy for the degree of serpentinization of a peridotite [*Christensen*, 1978]. The empirical formula derived for a set of ophiolitic and abyssal serpentinized peridotites by combining density measurements and modal analysis of the serpentine fraction (S) is d (grain density of sample in g/cm^3) = 3.300 − 0.785*S [*Miller and Christensen*, 1997]. This empirical formula is similar to the theoretical formula calculated from mineral densities for a typical residual harzburgitic composition (80% olivine Fo_{90}; 20% orthopyroxene En_{90}; d = 3.326 − 0.777*S). The effect of spinel (density ~4.010 g/cm^3 for a Cr # of 0.3 and a Mg # of 0.7, where Cr # = Cr/(Cr + Al) and Mg # = Mg/(Mg + Fe)) can be neglected because this accessory mineral forms less than 2% of the rock. Magnetite formed during serpentinization (density ~5.200 g/cm^3), however, makes up to 8% of our samples (Figure 7) and can therefore bias calculated serpentine fractions [*Miller and Christensen*, 1997]. To correct for this bias, we have calculated corrected density values (d_c) such that $d_c = (d - m*5.200)/(1 - m)$. We then used d_c to calculate serpentine fractions using *Miller and Christensen*'s [1997] empirical formula.

4.5.1. Magnetite content and the degree of serpentinization. [37] Figure 8 shows the evolution of Js with grain densities (d and d_c) for 27 samples from sites 395, 670, 895, and 920. In Figure 8b we plotted Js and calculated d_c values (d_c = 3.300 – 0.785*S) for nine samples, 100% serpentinized, from the tortoise shell textured interval at site 670. These samples, whose magnetic properties had been measured by *Bina et al.* [1990], were then cut to make thin sections, and we could not therefore measure their density.

[38] Js values and magnetite contents are low (Js < 1 A m^2/kg and m < 1%) in high-density samples, corresponding to low to moderate degrees of serpentinization (d_c > 2.700 g/cm^3 or S < 75%). Figure 8a shows a great scatter of Js values for uncorrected sample densities d < 2.750 g/cm^3. This scatter is

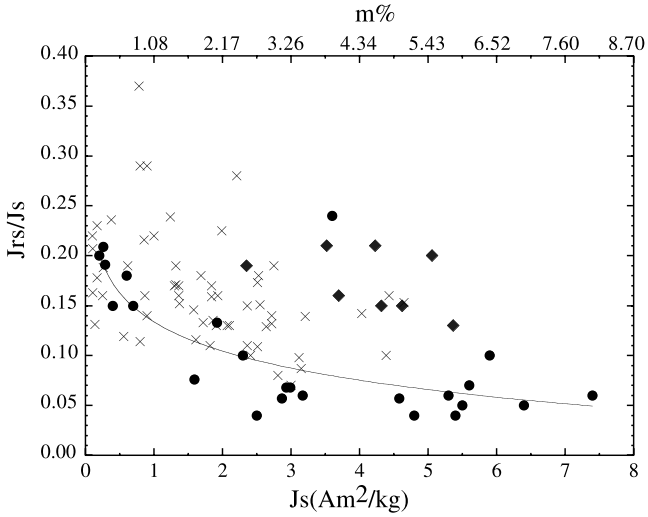

Figure 7. Jrs/Js as a function of Js and of the amount of magnetite (m%) in serpentinized peridotites from ODP sites 670, 920, and 895. A mediocre correlation (line shows best fit for a power law dependence; R = 0.76) is observed between these parameters for ODP site 670 samples. Symbols are the same as in Figure 3.

reduced in Figure 8b, which shows a rapid increase of Js (i.e., of the magnetite content) as corrected density decreases, for d_c < 2.700 g/cm^3 or S > 75%. At site 895 the best fitting trend corresponds to the relation: $\log_{10}$ (Js) = 11.38−4.34*d_c (R = 0.91). Using the Js versus m relationship derived in section 4.4.1 and *Miller and Christensen*'s [1997] relationship between d_c and S, this best fitting trend becomes: $\log_{10}$ (m) = 3.406*S − 4.903.

[39] Most samples from sites 670 and 920 have higher Js values (i.e., higher magnetite contents) at a given corrected density (i.e., at a given degree of serpentinization) than samples from site 895 (Figure 8b). This indicates that the rate of production of magnetite during serpentinization was lower at site 895 than at the other two sites. Figure 9 puts this conclusion into perspective, however, by comparing the trend of K (linearly correlated with Js in our samples; see Figure 5) versus density (d) at site 895, with that determined by *Toft et al.* [1990] for a set of ophiolitic samples ($\log_{10}$ (K) = 3.28 − 1.95*d). Although K values tend to be smaller for a given sample density at site 895 than at sites 670 and 920, they are higher than observed in Toft et al.'s ophiolitic sample set. The best fitting trend (R = 0.74) for site 895 in Figure 9 corresponds to the relation: $\log_{10}$ (K) = 9.80 − 4.25*d.

4.5.2. Magnetic grain size and the degree of serpentinization. [40] There is no evidence in the data listed in Table 1 for a dependence of Jrs/Js (i.e., of the magnetic grain size) on the corrected density (i.e., on the degree of serpentinization) of our samples.

5. Mineralogy and Iron Content of Secondary Silicates in the Serpentine Meshwork

[41] Serpentinization of olivine can be described by the simplified formula

$$\text{olivine} + H_2O = \text{serpentine} \pm \text{brucite} \pm \text{magnetite}.$$

The quantity of magnetite formed, hence the magnetic properties of serpentinized peridotites, is largely controlled by the ability of iron released by altered olivine to enter the structure of secondary silicates such as serpentine minerals and brucite. In order to test this ability and to determine how it varies from one site to another and how it evolves with the degree of serpentinization, we have performed microprobe analyses of primary and secondary silicates in our 54 thin sections (see Table 1). We have also selected 13 extensively serpentinized samples (1 from site 395, 3 from site 670, 2 from site 895, and 5 from site 920) for X-ray analyses of powders made from the serpentine meshwork.

5.1. Mineralogy of the Serpentine Meshwork

[42] X-ray diffraction analyses of serpentine meshwork separates from 13 selected samples show similar mineralogies and

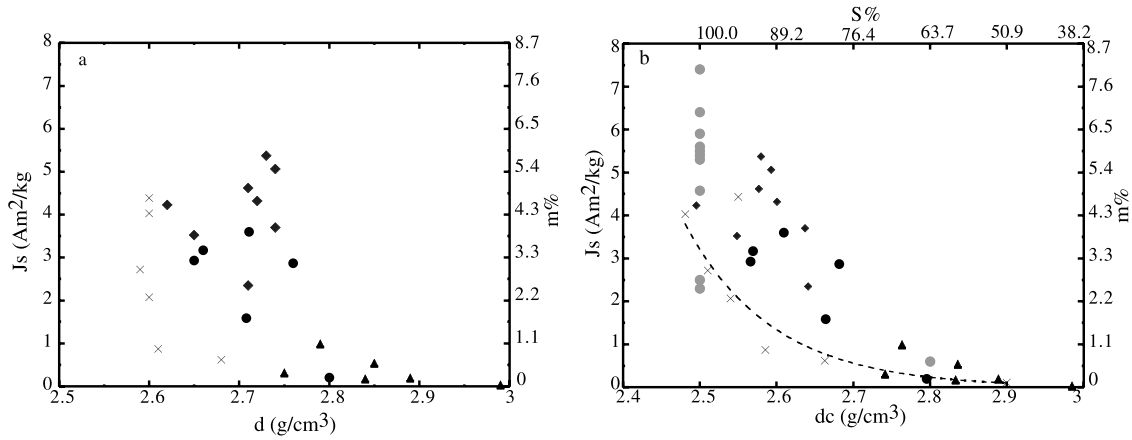

Figure 8. Variation of saturation magnetization Js (amount of magnetite or magnetite+maghemite in sample, m%) with grain density of serpentinized abyssal peridotites. (a) Density d not corrected of the effect of magnetite (or magnetite + maghemite) content. (b) Density corrected of the effect of magnetite (or magnetite + maghemite) contents (d_c). Degree of serpentinization (S%) is calculated using *Miller and Christensen*'s [1997] empirical formula. Dashed line shows best fitting relationship between Js and d_c for ODP site 895 samples (see text). Shaded dots correspond to densities calculated using *Miller and Christensen*'s [1997] formula (see text) for 100% serpentinized samples from site 670 and for two partially serpentinized samples (one from site 670 and the other from site 895). The d_c values <2.515 g/cm^3, corresponding to 100% serpentinized samples using *Miller and Christensen*'s [1997] empirical formula, in two samples may be a consequence of porosity, which was not completely saturated during density measurements.

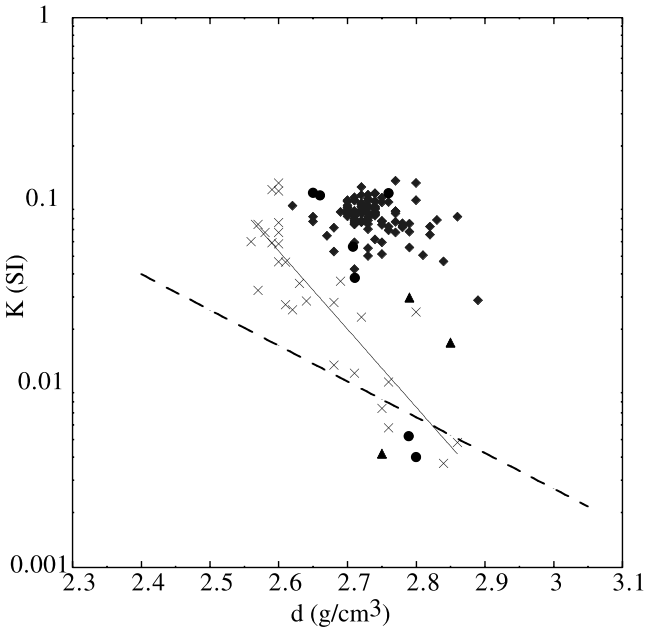

Figure 9. Magnetic susceptibility (K) as a function of grain density (d) in serpentinized peridotites from ODP sites 395, 670, 920, and 895. Solid line shows best fitting relation between K and d in samples from ODP site 895 samples ($\log_{10}$ (K) = 9.80−4.25*d; R = 0.74). Dashed line shows best fitting relation found by *Toft et al.* [1990] for a set of ophiolitic samples ($\log_{10}$ (K) = 3.28 − 1.95*d). Symbols are the same as in Figure 3.

indicate a lizardite + chrysotile dominated mixture at all sites. Most samples from sites 670 and 895 also contain brucite, characterized by reflections at d(Å) = 4.78 – 4.77, 2.36, and 1.48. One sample from site 895 shows weak antigorite reflections at d(Å) = 1.81, and 1.56 – 1.57 [*Whittaker and Zussman*, 1956; *Wicks and O'Hanley*, 1988]. Antigorite was also detected in serpentinized peridotites from this site by *Früh-Green et al.* [1995], using high-resolution transmission electron microscopy (HRTEM).

[43] Laboratory serpentinization experiments have shown that lizardite is the most abundant serpentine polymorph formed in the early stages of serpentinization [*Moody*, 1976; *Caruso and Chernosky*, 1979; *O'Hanley and Dyar*, 1998]. As serpentinization proceeds, this early formed lizardite appears to be replaced by chrysotile. Numerous studies [*Page*, 1968; *Whittaker and Wicks*, 1970; *Wicks and Plant*, 1979; *O'Hanley and Dyar*, 1993, 1998] have shown that lizardite can incorporate more iron in its structure than chrysotile. Destabilization of lizardite as serpentinization proceeds may thus cause iron to be freed to form magnetite [*O'Hanley and Dyar*, 1993, 1998]. Unfortunately, X-ray data do not allow us to quantify the respective proportions of lizardite and chrysotile in our abyssal samples. This is one of the objectives of an infrared spectroscopy protocol that is currently being developed, using some of our samples as test cases (C. Lemaire et al., Vibrational spectroscopy: A convenient tool for identification and characterization of transformation sequences among varieties of serpentines, submitted to *Canadian Mineralogist*, 2000).

5.2. Iron Content in Secondary Silicates

[44] Table 2 shows selected average compositions of serpentine and serpentine-brucite assemblages, formed after olivine in moderately to extensively serpentinized peridotites from sites 395, 670, 895, and 920. Figure 10 shows average iron contents in serpentine and in relicts of olivine and orthopyroxenes in partially serpentinized samples. FeO contents of relics olivine and orthopyroxenes vary little between samples (8.9–10.4 and 5.5–6.5 wt %, respec-

Table 2. Representative Microprobe Analyses of Serpentine After Olivine in Partially (Analyses 1–3) to Extensively (Analyses 4–12) Serpentinized Peridotite Samples[a]

	Analyses																							
	1		2		3		4		5		6		7		8		9		10		11		12	
	Site 395 18R1 (118–120) 6[b]		Site 670 6R1 (0–4) 4[b]		Site 895D 5R2 (41–43) 6[b]		Site 556 20R2 (20–24) 4[b]		Site 558 41R3 (113–115) 4[b]		Site 560 5R1 (98–101) 4[b]		Site 395 4R2 (64–66) 6[b]		Site 670 5R1(104–106) 14[b]		Site 920B 7R2 (42–44) 13[b]		Site 920D 14R5 (69–71) 7[b]		Site 895E[a] 7R2 (94–96) 10[b]		Site 895E[a] 7R1(116–120) 6[b]	
	Mean	SD	Mean	SD	Mean	SD	Mean	SD	Mean	SD	Mean	SD	Mean	SD	Mean	SD	Mean	SD	Mean	SD	Mean	SD	Mean	SD
CL	0.18	0.12	0.47	0.23	–	–	–	–	–	–	–	–	0.10	0.01	0.05	0.02	0.04	0.03	0.10	0.06	–	–	–	–
CaO	0.04	0.03	0.09	0.05	0.05	0.02	0.14	0.07	0.05	0.02	0.04	0.01	0.03	0.02	0.04	0.03	0.03	0.02	0.02	0.02	0.03	0.02	0.04	0.03
TiO_2	0.01	0.01	0.00	0.01	0.02	0.02	0.00	0.05	0.01	0.02	0.06	0.02	0.02	0.02	0.01	0.02	0.02	0.03	0.03	0.03	0.03	0.03	0.01	0.02
Cr_2O_3	0.01	0.01	0.03	0.06	0.03	0.05	0.03	0.03	0.02	0.01	0.06	0.06	0.01	0.01	0.01	0.01	0.02	0.03	0.04	0.04	0.02	0.04	0.02	0.05
MnO	0.05	0.07	0.11	0.07	0.09	0.12	0.01	0.01	0.02	0.21	0.05	0.04	0.03	0.04	0.10	0.06	0.07	0.07	0.09	0.07	0.11	0.09	0.47	0.09
FeO	6.91	1.05	5.45	0.41	5.39	1.17	3.21	2.21	2.8	0.32	2.34	1.48	1.85	0.17	2.68	1.21	1.95	0.57	2.42	0.48	4.68	0.87	13.19	2.55
NiO	0.25	0.13	0.24	0.11	0.27	0.13	0.2	0.16	0.25	0.09	0.36	0.09	0.22	0.06	0.21	0.15	0.22	0.10	0.19	0.16	0.38	0.15	0.44	0.16
Na_2O	0.02	0.01	0.07	0.04	0.02	0.01	0.01	0.05	0.01	0.02	0.02	0.02	0.02	0.01	0.01	0.01	0.02	0.02	0.04	0.02	0.01	0.01	0.00	0.01
SiO_2	38.92	1.54	37.8	1.53	38.12	3.26	43.2	2.53	40.96	1.01	42.84	1.14	42.06	0.57	41.4	2.26	41.6	0.68	41.19	0.84	39.03	2.09	15.97	4.48
MgO	37.80	1.64	36.94	1.67	38.63	0.62	41.21	1.51	38.37	0.76	39.24	2.40	39.06	0.59	39.48	0.84	39.88	0.69	39.6	0.63	39.18	0.55	44.81	1.39
Al_2O_3	0.21	0.36	0.05	0.04	0.02	0.03	0.02	0.02	0.21	0.05	0.43	0.25	0.63	0.08	0.04	0.06	0.54	0.36	0.60	0.26	0.02	0.03	0.01	0.01
Total	84.39		81.27		82.62		88.01		82.65		85.29		84.03		84.02		84.4		84.34		83.5		75.11	

[a] The composition of serpentine-brucite intergrowths in extensively serpentinized samples. Each composition is the average of 4–14 individual analyses.
[b] Number of points analyzed.

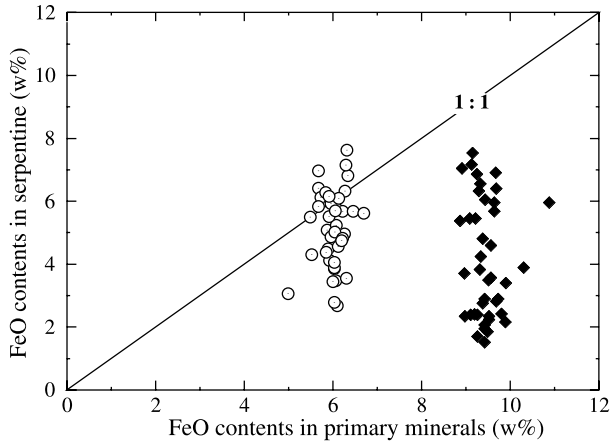

Figure 10. FeO content in serpentine as a function of the FeO content of olivine (solid diamonds) and orthopyroxene (open dots) in partially serpentinized samples from the seven studied drill sites. Each point corresponds to one sample and to the average of 4–14 microprobe measurements.

tively). Average FeO contents of serpentine formed after these two primary minerals are, by contrast, very variable from one sample to another. The range of FeO variations is relatively small within individual samples (see standard deviation (SD) values in Table 2), the wide range of FeO values shown in Figure 10 therefore mostly reflects between samples variations. Serpentines formed after olivine contain 1.5–8 wt % FeO (Figure 10), corresponding to significant iron losses compared with their parent mineral. Serpentines after orthopyroxene (bastite) have similar or slightly higher FeO contents, corresponding to little or no loss of iron compared with their parent mineral. Iron released during serpentinization therefore chiefly comes from the alteration of olivine.

[45] X-ray analyses show that some samples from sites 670 and 895 also contain brucite. This mineral occurs as poorly crystallized grains mixed with serpentine. At site 895 these brucite-serpentine assemblages are common (Figure 2c) and characterized by high FeO contents (8–16 wt %, Table 2), high MgO contents (42–52 wt %), and low SiO_2 contents (10–29 wt %). In a MgO-SiO_2-FeO ternary diagram these analyses plot on a mixing line between serpentine and iron-rich (FeO ~ 30 wt %) brucite. We have not detected the presence of brucite in microprobe analyses of samples from site 670. This suggests that this mineral, although detected in X-ray patterns, is not present in sufficient amounts to affect the composition of the serpentine. We have also not detected brucite in the two site 920 samples selected for X-ray analyses, yet *Dilek et al.* [1997] proposed that anomalously low SiO_2 contents measured in serpentines from these sites could be due to the presence of mixed brucite. Whatever the case, these analyses do not show anomalously high iron contents. Brucite, if present at site 920, is therefore presumably iron-poor.

5.3. Iron Content in Serpentine and the Degree of Serpentinization

[46] Figure 11 shows the average FeO contents in serpentine after olivine, the corrected density (d_c) and the calculated degree of serpentinization (S, in %) for the 54 samples selected for thin section analyses. Serpentine FeO contents are high (>5 wt %) in samples that are less than ~75% serpentinized (d_c > 2.750 g/cm^3). This represents a moderate loss of iron compared with parent olivines (Figure 10); magnetite is thus expected to have formed at a relatively modest rate in these partially serpentinized samples. Serpentine FeO contents are, by contrast, low (<3.5 wt %) in extensively serpentinized samples (S > 75%; d_c > 2.750 g/cm^3) from sites 556, 558, 560, 670, and 920. Intrasample variations of these values are relatively small (see SD values in Table 2). This shows that iron-rich serpentines formed at earlier stages of the serpentinization process are not preserved but are effectively replaced by iron-poor serpentine. Magnetite may thus be expected to have formed at a fast rate in these extensively serpentinized samples, because iron-poor serpentine replaced both what olivine still remained, and previously formed iron-rich serpentine.

[47] In extensively serpentinized samples from site 895 and in one extensively serpentinized sample from site 395, serpentine after olivine contains >3.5 wt % FeO (Figure 11). In the case of site 895 samples these high FeO contents are probably due to small amounts of iron-rich brucite, mixed with serpentine [*Früh-Green et al.*, 1996]. In the case of the sample from site 395, high serpentine FeO contents may be due to the presence of minute iron oxide grains formed during the low-temperature alteration of magnetite.

6. SEM Images of Magnetite Grains and Clusters of Grains

[48] We analyzed scanning electron microscopy (SEM) images obtained on a set of 12 samples representative of 100% serpentinized peridotites from sites 670, 895, and 920 (Table 3). SEM images do not allow us to distinguish between individual grains of magnetite and clusters of adjacent grains. The results shown in Table 3 may therefore not be used to characterize the size and shape of magnetic grains in our samples. They do, however, allow us to relate the magnetic properties of our samples to the actual distribution and morphology of magnetite grains or clusters of grains in the serpentine matrix.

[49] The enlargement factor (500) was chosen as the best compromise to image small magnetite grains and clusters (pixel size of 0.34 by 0.34 μm) and to cover a sufficient portion of each thin section (image size of 174 by 174 μm). The SEM

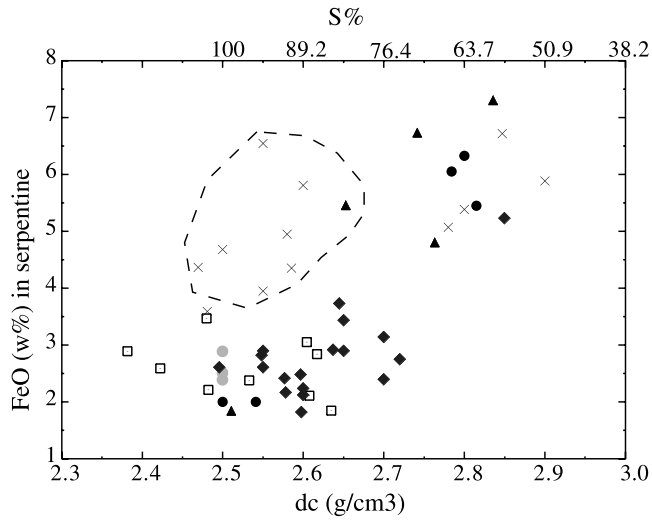

Figure 11. FeO content in serpentine as a function of the corrected grain density (d_c, proportional to the degree of serpentinization S (in %); see text) in 54 serpentinized peridotite samples from the seven studied drill sites. FeO value for each sample corresponds to the average of 4–14 microprobe measurements. Representative analyses are given in Table 2. High FeO contents in highly serpentinized samples (within dashed line) are attributed to mixture of serpentine with small amounts of iron-brucite and/or iron-oxides (see text). The d_c values <2.515 g/cm^3, corresponding to 100% serpentinized samples using *Miller and Christensen*'s [1997] empirical formula, in seven samples may be a consequence of porosity, which was not completely saturated during density measurements. Symbols are the same as in Figure 3.

Table 3. Morphological Parameters of Magnetite in 12 Completely Serpentinized Samples From ODP Sites 670, 895, and 920[a]

			Magnetite		Equivalent Diameter D			Elongation Ratio F				
										Mean F		
ODP Hole	Sample Core	Sample Interval, cm	Nb	Modal %	Mean D	SD	Magn. With D < Mean D, %	Mean F	SD	$D < 5$	$D > 10$	Magn. With $F < 0.2$, %
670[b]	5R1	104–106	1749	5.50	2.55	2.99	9.64	0.68	0.18	0.69	0.51	0.22
670[b]	5R1	114–116	1650	9.93	3.57	4.0	7.18	0.66	0.17	0.68	0.52	0.18
670[b]	5R1	135–138	750	7.49	4.67	5.07	5.81	0.67	0.17	0.68	0.61	0.05
670[b]	5R2	5–7	1791	11.32	2.78	4.26	5.42	0.64	0.17	0.65	0.52	0.43
670[b]	5R2	53–55	1152	7.7	2.39	2.35	10.59	0.62	0.17	0.63	0.56	0.73
670	9R1	12–14	1967	3.08	1.81	1.7	13.23	0.56	0.19	0.57	0.47	4.61
895E	3R3	16–18	2525	6.63	2.27	2.74	8.34	0.53	0.19	0.54	0.43	10.43
895E	5R2	41–43	1732	4.59	2.04	2.7	8.61	0.55	0.19	0.56	0.49	6.75
895E	6R2	112–114	1180	3.26	1.96	3.64	7.15	0.54	0.18	0.55	0.55	2.31
920B	1W3	46–48	5573	9.14	1.9	2.05	10.72	0.61	0.19	0.63	0.43	11.21
920D	4R1	22–24	1985	6.51	2.4	2.9	6.96	0.59	0.19	0.60	0.43	3.14
920D	21R1	103–105	950	4.35	2.62	3.61	6.9	0.54	0.20	0.57	0.31	20.64

[a] Nb, number of magnetite grains or clustered grains analyzed in each samples; modal %, modal proportion of magnetite in each sample, as determined from the cumulated surface of analyzed magnetite; D, equivalent diameter of magnetite grains and clusters of grains (see text); F, ratio of minor and major axis of ellipsoid that best fits the shape of magnetite surfaces; Nb, modal %, and D are determined only for magnetite with $D > 0.54$ μm; F is determined only for magnetite with $D > 0.77$ μm.

[b] Data for samples with large effective magnetic grain sizes (i.e., low Jrs/Js ratios).

images were binarized (serpentine in white; magnetite in black; Figure 12) and then analyzed using the NIH image software to determine the outline of magnetite grains and clusters of grains. We used ~15 images per sample, covering a surface of ~0.45 mm^2, and focusing on magnetite-rich areas in order to image a large number of magnetite grains and clusters of grains in each sample (see Table 3). This approach is not designed to estimate the amount of magnetite in each sample, yet modal abundances of magnetite in our images do roughly correlate with magnetite contents calculated for the same samples using Js values (Tables 1 and 3). We did not analyze a set of orthogonal thin sections for each sample because not enough material was available to cut these thin sections. We checked, however, that our images do not reveal systematic preferred orientations of magnetite grains and clusters of grains at the sample scale.

[50] The surface (S) of each magnetite grain or cluster of grains is expressed in Table 3 as an equivalent diameter D ($D = (4*S/\pi)^{1/2}$). D is measured only for magnetite surfaces larger than 2 pixels ($D > 0.54$ μm). Our detection limit is therefore well above the theoretical and experimental size limit for single-domain (SD) magnetites (~0.05–0.08 μm [*Dunlop*, 1973; *Butler and Banerjee*, 1975]). The other parameters measured are the length of the minor (a)

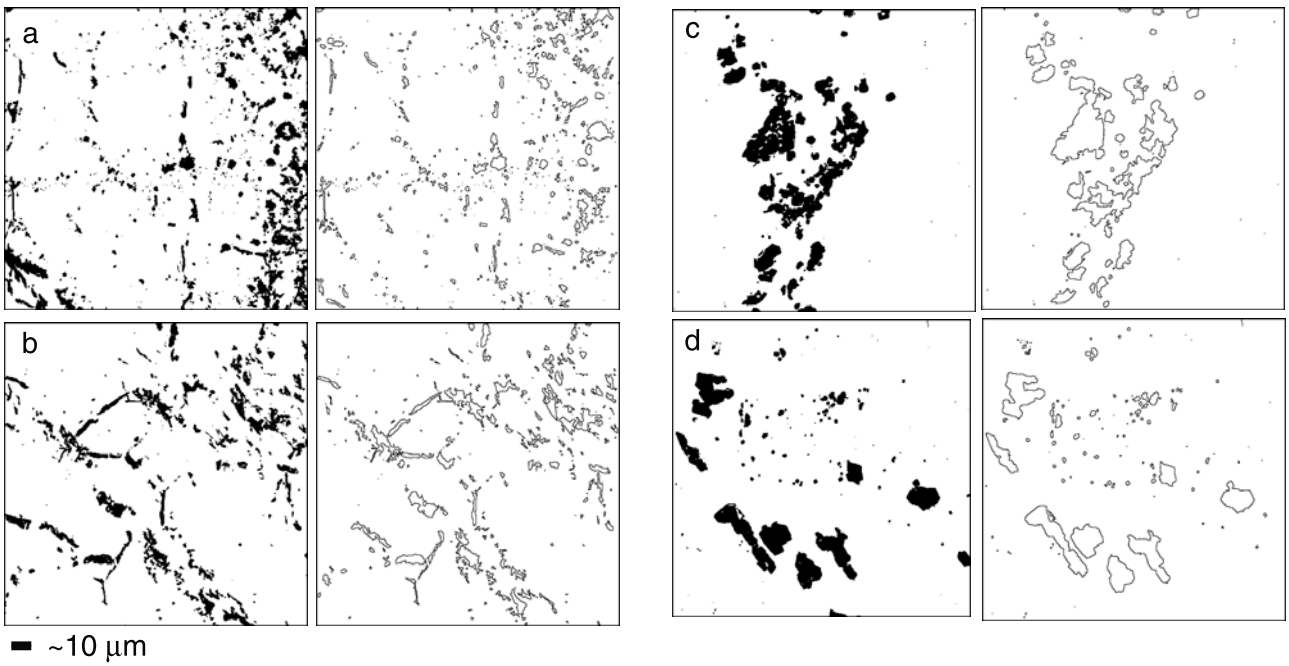

Figure 12. Examples of (left) binarized SEM images and (right) corresponding outlines of magnetite grains and clusters of grains analyzed with the NIH image software. (a) Image from sample 920D 4R1, 22–24 cm; (b) image from sample 895E 3R3, 16-18 cm; (c) image from sample 670 5R1, 114–116 cm; (d) image from sample 670 5R1, 104–106 cm. Image size is 174 by 174 μm.

and major (A) axes of the best fitting ellipsoid. These parameters and the elongation ratio F ($F = a/A$) are calculated only for magnetite surfaces larger than 4 pixels ($D > 0.77$ μm).

[51] The equivalent diameter (D) of imaged magnetite surfaces ranges from the detection limit (0.54 μm), up to ~50 μm. Because of the large number of very small magnetite surfaces, mean D values range between 1.8 and 4.7 μm, within the range of pseudo-single-domain (PSD) magnetite grain sizes [*Day et al.*, 1977; *Dunlop*, 1981]. Standard deviation values, however, are large, and magnetite surfaces with D equal to or smaller than these mean values represent <10% of the modal amount of magnetite in most samples (Table 3). Elongation ratios F vary between 0.1 (very elongated) and 1 (circular), with mean values between 0.53 and 0.68 (Table 3). Larger magnetite surfaces ($D > 10$ μm) in all samples are on average more elongated than smaller surfaces ($D < 5$ μm, Table 3).

[52] Low Jrs/Js samples from site 670 have values of mean $F > 0.61$ (Table 3). Magnetite surfaces in these samples are therefore on average slightly less elongated than in high Jrs/Js samples from sites 670, 895, and 920. Direct observation of SEM images suggests that this slight difference in average elongation reflects a more fundamental difference in the distribution of magnetite between the two groups of samples. In high Jrs/Js samples (e.g. Figures 12a and 12b), magnetite occurs in the form of thin and close-spaced vein-like concentrations, in most cases outlining the serpentine meshwork. Quite a few magnetite surfaces in these samples have a strong shape anisotropy ($F < 0.2$, Table 3). In low Jrs/Js samples, such strongly elongated magnetite surfaces represent <1% of the total magnetite (Table 3), and magnetite forms irregular aggregates, commonly near magnetite-free veins of serpentine (Figure 2d).

7. Discussion and Conclusions

7.1. Serpentinization and the Magnetic Properties of Abyssal Peridotites

7.1.1. Degree of serpentinization, iron content of secondary silicates, and amount of magnetite. [53] The amount of magnetite is linearly correlated with the magnetic susceptibility of serpentinized abyssal peridotites. It does not increase linearly with the degree of serpentinization (S) but remains modest in partially serpentinized samples ($S < 75\%$) and increases rapidly for higher degrees of serpentinization (>75%). This delay in the formation of magnetite is related to the iron content of serpentine minerals: In the first stages of serpentinization, iron released by primary silicates (mainly olivine) is largely used to form iron-rich (~6% FeO) serpentine, with small quantities of magnetite. As serpentinization proceeds beyond $S \sim 75\%$, this iron-rich serpentine (presumably lizardite) is destabilized to form iron-poor (2–3% FeO) serpentine (presumably chrysotile), and larger amounts of magnetite do crystallize. The amount of magnetite also depends on the formation of other iron-bearing secondary silicates, such as iron-brucite. Highly serpentinized samples from ODP site 895 contain less magnetite than similarly serpentinized samples from ODP sites 670 and 920. This difference is probably due to the crystallization of iron-rich brucite in the serpentine mesh of site 895 samples.

7.1.2. Magnetic grain sizes, and the distribution of magnetite in the serpentine meshwork. [54] The remanent properties of serpentinized abyssal peridotites are highly variable. For similar values of K, some samples have NRM values comparable to those of basalts (~20 A/m), while other samples have low NRM values (<5 A/m), yielding low values of the Koenigsberger ratio (Q). The study of magnetic hysteresis parameters shows that these contrasting remanent behaviors are due to differences in the effective magnetic grain sizes. Samples with high NRM values have Jrs/Js and Hcr/Hc values in the pseudo-single-domain (PSD) range, comparable to those of many basalts. Samples with low NRM values have Jrs/Js and Hcr/Hc values typical of the transition between PSD and MD magnetites.

[55] The analysis of magnetite distribution using SEM images shows that in samples with small effective magnetic grain sizes (high Jrs/Js ratio), magnetite occurs in the form of thin and close-spaced vein-like concentrations, in most cases outlining the serpentine meshwork. This texture could be favorable to the growth of elongated magnetites with enhanced coercivities [*Özdemir and Dunlop*, 1992]. By contrast, in samples with large effective magnetic grain sizes, magnetite forms irregular aggregates, with high magnetite concentrations (Figure 12d) that could promote strong magnetostatic interactions between the grains. Theoretical and experimental studies have shown that magnetostatic fields due to the interaction of SD grains act as demagnetizing fields and may therefore reduce the coercivity [*Dunlop and West*, 1969; *Shcherbakov and Shcherbakova*, 1977; *Dankers*, 1981; *Shcherbakov et al.*, 1995]. There are no equivalent studies of PSD aggregates, but it is likely that magnetostatic interactions between PSD grains can also reduce their coercivity.

[56] All samples with large effective magnetic grain sizes come from the tortoise shell textured interval at ODP site 670. The texture of this interval, characterized by widely spaced serpentine veins, the absence of a serpentine mesh texture, and the lack of bastites, is unusual among abyssal serpentinized samples. We therefore propose that samples with small effective magnetic grain sizes, being characterized by the more common serpentine meshwork texture, are more representative of the magnetic behavior of abyssal peridotites.

[57] The uneven distribution of magnetite in tortoise shell textured samples from site 670 indicates that iron released by the alteration of olivine migrated greater distances before it formed magnetite in these samples (the average spacing of serpentine veins rimmed with magnetite is ~4 mm) than in the more common mesh-textured samples (typical sizes for the serpentine meshwork are 0.5–1 mm). One explanation, suggested by the very localized nature of the tortoise shell textured interval at site 670 (6 m thick at most) is that this interval was a zone of high fluid flow during serpentinization, promoting high iron diffusion rates and either preventing the formation of a serpentine meshwork or causing it to be destroyed as serpentinization proceeded.

7.1.3. Near seafloor low temperature oxidative alteration. [58] Samples from DSDP sites 395, 556, 558, and 560 have a brecciated texture (detritic or cataclastic in origin) and have suffered varying degrees of low-temperature oxidative alteration. Magnetite in these samples is partially altered to maghemite. The NRM and the magnetic susceptibility of these samples are low. Dredged abyssal peridotite samples also commonly show evidence for low temperature oxidative alteration [*Oufi*, 2000], while samples drilled very near the seafloor at ODP sites 895 and 920 do not. This leads us to propose that this alteration normally occurs only within a few meters of the seafloor. Maghemitized drilled samples from DSDP site 395 are detritic breccias that formed on the seafloor and were subsequently buried by lava flows and sediments. Maghemitized drilled samples from DSDP sites 556, 558, and 560 are cataclastic breccia that formed in faults cutting into the ultramafic basement. These faults may have provided pathways for seawater to alter this basement.

7.2. Contribution of Serpentinized Peridotites to Marine Magnetic Anomalies

[59] The contribution of abyssal peridotites to marine magnetic anomalies can become significant (i.e., NRM values > 5 A/m) when they are affected by a high degree of serpentinization (>75%). Such highly serpentinized peridotites are characterized by seismic velocities (V_p) of 5–5.5 km/s [*Christensen*, 1978; *Horen et al.*, 1996; *Miller and Christensen*, 1997]. Such low velocities are modeled only down to depths of 1.5–2 km in the axial discontinuity of the MAR at 35°N [*Canales et al.*, 2000],

where serpentinized peridotites have been dredged [*Gracia et al.*, 1999]. Bodies of extensively serpentinized peridotites may be present below these depths but should be small (i.e., not resolvable with seismic tomography). It is therefore likely that only those highly serpentinized peridotites that are present in the first 1.5–2 km of the oceanic crust can contribute significantly to marine magnetic anomalies.

[60] The remanent magnetization carried by these highly serpentinized peridotites can be similar to that of oceanic basalts. Their induced magnetization, however, will generally be much higher than that of basalts. This is consistent with the interpretation proposed to explain the observed increase in the magnetization from center to end of many segments in the Mid-Atlantic Ridge axis [*Pariso et al.*, 1996; *Pockalny et al.*, 1995; *Tivey and Tucholke*, 1998; *Ravilly et al.*, 1998]. Off-axis, the effect of serpentinized peridotites should be an increase of total magnetization in normal polarity crust and a decrease of total magnetization in reverse polarity crust. It is indeed what is observed in the off-axis traces of several axial discontinuities near the Mid-Atlantic Ridge [*Pariso et al.*, 1996; *Pockalny et al.*, 1995; *Tivey and Tucholke*, 1998].

[61] Magnetic properties of extensively serpentinized peridotites can vary significantly depending on whether the samples have been maghemitized (on the seafloor or in a fault zone that provided a downgoing path to seawater), on whether the conditions of serpentinization allowed for the crystallization of iron-bearing silicates together with serpentine and magnetite (such as iron-rich brucite), and on whether these conditions of serpentinization favored the formation of a serpentine meshwork with thin vein-like concentrations of small and/or highly elongated magnetite grains. Our study of the seven existing DSDP and ODP drill sites in serpentinized peridotites leads us to propose that the magnetic properties of extensively serpentinized samples from ODP sites 895 and 920 (i.e., average NRM values of 4 or 10 A/m; average K values of 0.06 and 0.08 SI, respectively; and average Q values of 2 and 3.6, respectively) are representative of most highly serpentinized peridotites that could be present in the oceanic crust, outside fault zones, and more than a few meters below seafloor. These samples have a well-developed serpentine mesh texture. Lower K and NRM average values in extensively serpentinized samples from ODP site 895 are explained by the formation of lesser amounts of magnetite in these samples due to the crystallization of iron-rich brucite. Magnetic properties of serpentinized peridotites from the tortoise shell textured interval at ODP site 670 (average NRM value of 2.5 A/m and average K values of 0.12 SI) may be representative of rocks serpentinized in high fluid flow conditions. Low NRM values in these samples could be related to their unusual texture, which promotes the concentration of magnetite in irregular aggregates of moderately elongated and often relatively large grains.

[62] **Acknowledgments.** We thank the managers of ODP core repositories at Lamont and Bremen for their help in viewing cores and obtaining samples. M. Leikine helped us with X-ray analysis. C. Mével and J. Escartin read the manuscript at various stages and helped us with their comments. We also thank J. Gee, H.-U. Worm, and Associate Editor M. Tivey for their thorough reviews and helpful suggestions.

References

Agrinier, P., and M. Cannat, Oxygen isotopic constraints on serpentinization processes in ultramafic rocks from the Mid-Atlantic Ridge (lat. 23°N), in the MARK area, *Proc. Ocean Drill. Program Sci. Results*, *153*, 381–388, 1997.

Agrinier, P., R. Hekinian, D. Bideau, and M. Javoy, Stable isotope composition ($^{18}O/^{16}O$, D/H, and $^{14}C/^{12}C$) of oceanic crust and upper mantle rocks in the Hess Deep near the Galapagos Triple Juction, *Earth Planet. Sci. Lett.*, *136*, 183–196, 1996.

Arai, S., and T. Fujii, Petrology of ultramafic rocks from site 395, *Initial Rep. Deep Sea Drill. Proj.*, *45*, 587–594, 1978.

Argyle, K. S., and D. J. Dunlop, Low-temperature and high-temperature hysteresis of small multidomain magnetites (215–540 nm), *J. Geophys. Res.*, *95*, 7069–7083, 1990.

Argyle, K. S., D. J. Dunlop, and S. Xu, Single-domain behaviour of multidomain magnetite grains (abstract), *Eos Trans. AGU*, *75*(44), Fall Meet. Suppl.196, 1994.

Bina, M. M., and B. Henry, Magnetic properties, opaque mineralogy and magnetic anisotropies of serpentinized peridotites from ODP Hole 670A near the Mid-Atlantic Ridge, *Phys. Earth Planet. Inter.*, *65*, 88–103, 1990.

Bina, M. M., Y. Hamano, K. Krammer, and A. Wooldridge, Paleomagnetisme of basalts from ODP hole 648B on the Mid-Atlantic Ridge, *Proc. Ocean Drill. Program Sci. Results*, *106/109*, 291–295, 1990.

Bougault, H., et al., *Initial Reports of the Deep Sea Drilling Project*, vol. 82, U.S. Govt. Print. Off., 1985.

Butler, R. F., and S. K. Banerjee, Theoretical single-domain grain-size range in magnetite and titanomagnetite, *J. Geophys. Res.*, *80*, 4049–4058, 1975.

Canales, J. P., R. S. Detrick, J. Lin, J. A. Collins, and D. R. Toomey, Crustal and upper mantle seismic structure beneath the rift mountains and across a nontransform offset at the Mid-Atlantic Ridge (35°N), *J. Geophys. Res.*, *105*, 2699–2719, 2000.

Cannat, M., Emplacement of mantle rocks in the seafloor at mid-ocean ridges, *J. Geophys. Res.*, *98*, 4163–4172, 1993.

Cannat, M., et al., *Proceedings of the Ocean Drilling Program, Initial Reports*, vol. 153, Ocean Drill. Program, College Station, Tex., 1995.

Cannat, M., Y. Lagabrielle, H. Bougault, J. Casey, N. De Coutures, L. Dmitriev, and Y. Fouquet, Ultramafic and gabbroic exposures at the Mid-Atlantic Ridge: Geological mapping in the 15°N region, *Tectonophysics*, *279*, 193–213, 1997.

Caruso, L., and J. V. Chernosky Jr., The stability of lizardite, *Can. Mineral.*, *17*, 757–769, 1979.

Christensen, N. I., The abundance of serpentinites in the oceanic crust, *J. Geol.*, *80*, 709–719, 1972.

Christensen, N. I., Ophiolites, seismic velocities and oceanic crustal structure, *Tectonophysics*, *47*, 131–157, 1978.

Dankers, P., Relationship between median destructive field and remanent coercive forces for dispersed natural magnetite, titanomagnetite and hematite, *Geophys. J. R. Astron. Soc.*, *64*, 447–461, 1981.

Day, R., M. D. Fuller, and V. A. Schmidt, Hysteresis properties of titanomagnetites: Grain size and composition dependance, *Phys. Earth Planet. Inter.*, *13*, 260–267, 1977.

Day, R., S. Halgedahl, M. Steiner, K. Kobayashi, T. Furuta, T. Ishii, and A. Faller, Magnetic properties of basalts from DSDP Leg 49, *Initial Rep. Deep Sea Drill. Proj.*, *49*, 781–791, 1979.

Detrick, R., et al., *Proceedings of the Ocean Drilling Program, Initial Reports*, vol. 106/109, pp. 291–295, Ocean Drill. Program, College Station, Tex., 1988.

Dick, H. J. B., and J. H. Natland, Late-stage evolution and transport in the shallow mantle beneath the East Pacific Rise, *Proc. Ocean Drill. Program Sci. Results*, *147*, 103–134, 1996.

Dilek, Y., A. Coulton, and S. D. Hurst, Serpentinization and hydrothermal veining in peridotites at site 920 in the MARK area, *Proc. Ocean Drill. Program Sci. Results*, *153*, 35–59, 1997.

Dunlop, D. J., Hysteretic properties of synthetic and natural monodomain grains, *Philos. Mag.*, *19*, 329–338, 1969.

Dunlop, D. J., Superparamagnetic and single-domain threshold sizes in magnetite, *J. Geophys. Res.*, *78*, 1780–1793, 1973.

Dunlop, D. J., The rock magnetism of fine particles, *Phys. Earth Planet. Inter.*, *26*, 1–26, 1981.

Dunlop, D. J., Hysteresis properties of magnetite and their dependence on particle size: A test of pseudo-single-domain remanence models, *J. Geophys. Res.*, *91*, 9569–9584, 1986.

Dunlop, D. J., and Ö. Özdemir, *Rock Magnetism: Fundamentals and Frontiers*, 565 pp., Cambridge Univ. Press, New York, 1997.

Dunlop, D. J., and M. Prévot, Magnetic properties and opaque mineralogy of drilled submarine intrusive rocks, *Geophys. J. R. Astron. Soc.*, *69*, 763–802, 1982.

Dunlop, D. J., and G. F. West, An experimental evaluation of single domain theories, *Rev. Geophys.*, *7*, 709–757, 1969.

Dyment, J., and J. Arkani-Hamed, Spreading-rate-dependent magnetization of the oceanic lithosphere inferred from the anomalous skewness of marine magnetic anomalies, *Geophys. J. Int.*, *121*, 789–804, 1995.

Dyment, J., J. Arkani-Hamed, and A. Ghods, Contribution of serpentinized ultramafics to marine magnetic anomalies at slow and intermediate spreading centres: Insights from the shape of the anomalies, *Geophys. J. Int.*, *129*, 691–701, 1997.

Francheteau, J., R. Armijo, J. L. Cheminée, R. Hékinian, P. Lonsdale, and N. Blum, 1 Ma East Pacific Rise oceanic crust and uppermost mantle exposed by rifting in Hess Deep (equatorial Pacific Ocean), *Earth Planet. Sci. Lett.*, *101*, 281–295, 1990.

Früh-Green, G. L., A. Plas, B. Grobéty, and C. Lécuyer, Multi-stage hydrothermal alteration and antigorite serpentinization of EPR shallow mantle at Hess Deep, *Terra Abstr.*, *7*, 208, 1995.

Früh-Green, G. L., A. Plas, and C. Lécuyer, Petrological and stable isotope constraints on hydrothermal alteration and serpentinization of the EPR shallow mantle at Hess Deep (site 895), *Proc. Ocean Drill. Program Sci. Results*, *147*, 255–291, 1996.

Ghose, I., M. Cannat, and M. Seyler, Transform fault effect on mantle melting in the MARK area (Mid-Atlantic Ridge south of the Kane transform), *Geology*, *24*, 1139–1142, 1996.

Gracia, E., D. Bideau, R. Hekinian, and Y. Lagabrielle, Detailed geological mapping of two contrasting second-order segments of the Mid-Atlantic Ridge between Oceanographer and Hayes fracture zones (33°30′N–35°N), *J. Geophys. Res.*, *104*, 22,903–22,922, 1999.

Hamano, Y., M. M. Bina, and K. Krammer, Paleomagnetism of the serpentinized peridotite from ODP Hole 670A, *Proc. Ocean Drill. Program Sci. Results*, *106/109*, 257–262, 1990.

Hébert, R., A. C. Adamson, and S. C. Komor, Metamorphic petrology of ODP leg 109, hole 670A, serpentinized peridotites: Serpentinization processes at a slow spreading ridge environment, *Proc. Ocean Drill. Program Sci. Results*, *106/109*, 103–106, 1990.

Heider, F., D. J. Dunlop, and N. Sugiura, Magnetic properties of hydrothermally recrystallized magnetite crystals, *Science*, *236*, 1287–1290, 1987.

Heider, F., A. Zitzelsberger, and K. Fabian, magnetic susceptibility and remanent coercivity force in grown magnetite crystals from 0.1 μm to 6 mm, *Phys. Earth Planet. Inter.*, *93*, 239–256, 1996.

Horen, H., and G. Dubuisson, Rôle de l'hydrothermalisme sur les propriétés magnétiques d'une lithosphère océanique formée à une ride lente: L'ophiolite de Xigaze (Tibet), *C. R. Acad. Sci., Ser. IIa*, *312*, 1095–1102, 1995.

Horen, H., M. Zamora, and G. Dubuisson, Seismic waves velocities and anisotropy in serpentinized peridotites from Xigaze ophiolite: Abundance of serpentine at slow spreading ridges, *Geophys. Res. Lett.*, *23*, 9–12, 1996.

Hornes, S., H. Friedrichsen, and H. H. Schock, Oxygen-and hydrogen-isotope and trace-element investigation on rocks of DSDP Hole 395A, *Initial Rep. Deep Sea Drill. Proj.*, *45*, 541–550, 1978.

Johnson, P. H., Rock magnetic properties of samples—DSDP Leg 45, *Initial Rep. Deep Sea Drill. Proj.*, *45*, 397–406, 1978.

Karson, J. A., S. D. Hurst, and P. Lonsdale, Tectonic rotation of dikes in fast-spread oceanic crust exposed near Hess Deep, *Geology*, *20*, 685–688, 1992.

Kelso, P. R., C. Richter, and J. E. Pariso, Rock magnetic properties, magnetic mineralogy and paleomagnetism of peridotite from site 895, Hess Deep, *Proc. Ocean Drill. Program Sci. Results*, *147*, 405–413, 1996.

Komor, S. C., D. Elthon, and F. J. Casey, serpentinization of cumulate ultramafic rocks the North Arm Moutain massif of the Bay of Islands ophiolite, *Geochim. Cosmochim. Acta*, *49*, 2331–2338, 1985.

Komor, S. C., T. L. Grove, and R. Hébert, Abyssal peridotites from ODP Hole 670A (21°10′N, 45°02′W): Residues of mantle melting exposed by non-constructive axial divergence, *Proc. Ocean Drill. Program Sci. Results*, *106/109*, 85–1001, 1990.

Krammer, K., Rock magnetic properties and opaque mineralogy of selected samples from Hole 670A, *Proc. Ocean Drill. Program Sci. Results*, *106/109*, 269–273, 1990.

Lagabrielle, Y., and M. Cannat, Alpine jurassic ophiolites resemble the modern central Atlantic basement, *Geology*, *18*, 319–322, 1990.

Lienert, B. R., and P. G. Wasilewski, A magnetic study of the serpentinization process at Burro Mountain, California, *Earth Planet. Sci. Lett.*, *43*, 406–416, 1979.

Melson, W. G., et al., *Initial Reports of the Deep Sea Drilling Project*, vol. 45, U.S. Govt. Print. Off., Washington, D. C., 1976. [Shipboard Scientific Party, 1976.]

Melson, W. G., P. D. Rabinowitz, J. H. Natland, H. Bougault, and H. P. Johnson, *Initial Reports of the Deep Sea Drilling Project*, *vol. 45*, pp. 587–594, U.S. Govt. Print. Off., Washington, D. C., 1978.

Mével, C., and C. Stamoudi, Hydrothermal alteration of the upper-mantle section at Hess Deep, *Proc. Ocean Drill. Program Sci. Results*, *147*, 293–309, 1996.

Mével, C., et al., *Proceedings of the Ocean Drilling Program, Initial Reports*, vol. 147, Ocean Drill. Program, College Station, Tex., 1993.

Michael, P. J., and E. Bonatti, Petrology of ultramafic rocks from sites 556, 558 and 560 in the North Atlantic, *Initial Rep. Deep Sea Drill. Proj.*, *82*, 523–528, 1985.

Miller, D. J., and N. I. Christensen, Seismic velocities of lower crustal and upper mantle rocks from the slow-spreading Mid-Atlantic Ridge, south of the Kane transform zone (MARK), *Proc. Ocean Drill. Program Sci. Results*, *153*, 437–454, 1997.

Moody, J., An experimental study on the serpentinization of iron-bearing olivines, *Can. Mineral.*, *14*, 462–478, 1976.

Nazarova, K. A., Serpentinized peridotites as a possible source for oceanic magnetic anomalies, *Mar. Geophys. Res.*, *16*, 455–462, 1994.

Niida, K., Mineralogy of MARK peridotites: Replacement through magma channeling examined from Hole 920D, MARK area, *Proc. Ocean Drill. Program Sci. Results*, *153*, 265–275, 1997.

O'Hanley, D. S., and M. D. Dyar, The composition of lizardite 1T and the formation of magnetite in serpentines, *Am. Mineral.*, *78*, 391–404, 1993.

O'Hanley, D. S., and M. D. Dyar, The composition of chrysotile and its relation with lizardite, *Can. Mineral.*, *36*, 727–739, 1998.

Oufi, O., Les propriétés magnétiques des péridotite serpentinisées abyssales: Relation entre la composition chimique, la nature minéralogique des minéraux serpentineux et le comportement magnétique des péridotites serpentinisées, Ph.D. thesis, 276 pp., Univ. Paris 7 Denis Diderot, Paris, 2000.

Özdemir, Ö., and D. J. Dunlop, Domain structure observations in biotite and hornblendes, *Eos Trans. AGU*, *73*(14), Spring Meet. Suppl., 93, 1992.

Page, N. G., Chemical differences among the serpentine "polymorphs," , *Am. Mineral.*, *53*, 201–215, 1968.

Pariso, J. E., C. Rommevaux, and J. C. Sempéré, Three-dimensional inversion of marine magnetic anomalies: Implications for crustal accretion along the Mid-Atlantic Ridge (28°–31°30′N), *Mar. Geophys. Res.*, *18*, 85–101, 1996.

Parry, L. G., Magnetic properties of dispersed magnetite powders, *Philos. Mag.*, *11*, 303–312, 1965.

Pockalny, R. A., A. Smith, and P. Gente, Spatial and temporal variability of crustal magnetization of a slowly spreading ridge: Mid-Atlantic Ridge (20°–24°N), *Mar. Geophys. Res.*, *17*, 301–320, 1995.

Rahman, A. A., A. D. Duncan, and L. G. Parry, Magnetization of multidomain magnetite particles, *Riv. Ital. Geofis.*, *22*, 259–266, 1973.

Ravilly, M., J. Dyment, P. Gente, and R. Thibaud, Axial magnetic anomaly amplitude along the Mid-Atlantic Ridge between 20°N and 40°N, *J. Geophys. Res.*, *103*, 24,201–24,222, 1998.

Richter, C., P. R. Kelso, and J. M. Christopher, Magnetic fabrics and sources of magnetic susceptibility in lower crustal and upper mantle rocks from Hess Deep, *Proc. Ocean Drill. Program Sci. Results*, *147*, 393–403, 1996.

Roest, W. R., J. Arkani-Hamed, and J. Verhoef, The seafloor spreading rate dependence of the anomalous skewness of marine magnetic anomalies, *Geophys. J. Int.*, *109*, 653–669, 1992.

Shcherbakov, V. P., and V. V. Shcherbakova, Calculation of thermoremanence and ideal magnetization of an ensemble of interacting single-domain grains, (translated from Russian), *Izv. Phys. Solid Earth, Engl. Transl.*, *18*, 413–421, 1977.

Shcherbakov, V. P., B. E. Lamash, and N. K. Sycheva, Monte Carlo modelling of thermoremanence acquisition in interacting single-domain grains, *Phys. Earth. Planet. Inter.*, *87*, 197–211, 1995.

Sinton, J. M., Petrology of alpine type peridotites from site 395, DSDP Leg 45, *Initial Rep. Deep Sea Drill. Proj.*, *45*, 595–601, 1978.

Smith, B. M., Consequences of the maghemitization on the magnetic properties of submarine basalts: Synthesis of previous works and results concerning basement rocks from mainly DSDP Legs 51 and 52, *Phys. Earth Planet. Inter.*, *46*, 206–226, 1987.

Smith, G. M., and S. K. Banerjee, Magnetic properties of plutonic rocks from the central North Atlantic Ocean, *Initial Rep. Deep Sea Drill. Proj.*, *82*, 377–383, 1985.

Stacey, F. D., A generalized theory of thermoremanence, covering the transition from single domain to multi-domain magnetic grains, *Philos. Mag.*, *7*, 1887–1900, 1962.

Stacey, F. D., and S. K. Banerjee, *The Physical Principles of Rock Magnetism*, 195 pp., Elsevier Sci., New York, 1974.

Stoner, E. C., and E. P. Wohlfarth, A mechanism of magnetic hysteresis in heterogeneous alloys, *Philos. Trans. R. Soc. London, Ser. A*, *240*, 599–642, 1948.

Talwani, M., C. C. Windisch, and M. G. Langseth, Reykjanes crest: A detailed geophysical study, *J. Geophys. Res.*, *76*, 473–517, 1971.

Tivey, M. A., and B. E. Tucholke, Magnetization of 0-29 Ma ocean crust on the Mid-Atlantic Ridge, 25°30′ to 27°10′N, *J. Geophys. Res.*, *103*, 17,807–17,826, 1998.

Toft, P. B., J. Arkani-Hamed, and S. E. Haggerty, The effects of serpentinization on density and magnetic susceptibility: A petrophysical model, *Phys. Earth Planet. Inter.*, *65*, 137–157, 1990.

Tucholke, B. E., and J. Lin, A geological model for the structure of ridge segments in slow spreading ocean crust, *J. Geophys. Res.*, *99*, 11,937–11,958, 1994.

Whittaker, E. J. W., and F. J. Wicks, Chemical differences among the serpentine "polymorphs": A discussion, *Am. Mineral.*, *55*, 1025–1047, 1970.

Whittaker, E. J. W., and J. Zussman, The characterization of serpentine minerals by X-ray diffraction, *Mineral. Mag.*, *31*, 107–126, 1956.

Wicks, F. J., and D. S. O'Hanley, Serpentines: Structure and petrology, in *Hydrous Phyllosilicates Exclusive of Micas*, *Rev. Mineral.*, vol. 19, edited by S. W. Bailey, pp. 91–168, Mineral. Soc. of Am., Washington, D. C., 1988.

Wicks, F. J., and G. Plant, Electron microphobe and X-ray microbeam studies of serpentine textures, *Can. Mineral.*, *17*, 785–830, 1979.

Wicks, F. J., and E. J. W. Whittaker, Serpentine textures and serpentinization, *Can. Mineral.*, *15*, 459–488, 1977.

Wohlfarth, E. P., Relations between different modes of acquisition of the remanent magnetization of titanomagnetic particles, *J. Appl. Phys.*, *29*, 595–596, 1958.

Worm, H. U., and H. Markert, Magnetic hysteresis properties of fine particle titanomagnetites precipitated in a silicate matrix, *Phys. Earth. Planet. Inter.*, *46*, 84–92, 1987.

M. Cannat and O. Oufi, Laboratoire de Géosciences Marine, Université Pierre et Marie Curie, CNRS/IPGP, 4 place Jussieu, F-75252 Paris cedex 05, France. (oufi@ccr.jussieu.fr; cannat@ccr.jussieu.fr)

H. Horen, Laboratoire de Géologie, ENS, 24 rue Lhomond, F-75231, Paris cedex 05, France.